University of California
Santa Barbara

Particle Migration and Focusing in Inertial Microfluidic Flows

A dissertation submitted in partial satisfaction
of the requirements for the degree

Doctor of Philosophy
in
Mechanical Engineering

by

Mike Garcia

Committee in charge:

Professor Sumita Pennthur, Chair
Professor L. Gary Leal
Professor Carl D. Meinhart
Professor Megan T. Valentine

December 2018

The Dissertation of Mike Garcia is approved.

Professor L. Gary Leal

Professor Carl D. Meinhart

Professor Megan T. Valentine

Professor Sumita Pennthur, Committee Chair

November 2018

Particle Migration and Focusing in Inertial Microfluidic Flows

To my parents Juan and Candida Garcia

Acknowledgements

I would like to give many thanks to the people that made this work possible. First, I would like to thank, Professor Sumita Pennthur, for all of her guidance and encouragement over the last four years. You pushed me to reach my fullest potential and you believed in me even when I did not believe in myself. My time at UCSB would have been very different without you, and I am proud of our work. I would like to thank my committee, Professor Megan Valentine, Professor Carl Meinhart, and Professor Gary Leal, for their suggestions, insight and advice. I would like to thank my collaborators Professor Baskar Ganapathysubramanian and Professor Dino Di Carlo, for taking an interest in my ideas and providing their expertise in the development of my work. It has been a great experience working with them and I hope that we can continue to collaborate in the future. I would also like to thank Professor Paulo Aratia, for his unwavering support. Paulo, was the first to truly believe in me and even though we could not finish what we started I am grateful that I had the opportunity to learn from him. Of course I would also like to thank all past and present members of the UCSB Nanolab. Jin, for the hours we spent procrastinating by eating snacks together. Chris, for always being so calm and composed. Travis, for being my first friend in Santa Barbara. Thank you also Maria, Alex, Pascal, Sean, Karen, Xavier, Tyler, Elijah, Nathaniel, Amanda, Kjeld, Tim, Kerry, and Seth. I would like to thank all of my friends outside of the lab for all of the fun times. I am grateful to my family, for their love and endless support during my academic pursuit. They have sacrificed so much for me and my dreams and for that I am forever thankful. Lastly, I would like to thank for my best friend, my Love, Alyssa Walter for her endless support and patience. I don't know if I could have done this without her. I am so thankful I had you through this experience and I am excited for what is in store for us next.

Curriculum Vitæ

Mike Garcia

Education

2014–2018	Ph.D. in Mechanical Engineering, University of California, Santa Barbara.
2010–2013	M.S. in Mechanical Engineering, University of Pennsylvania
2006–2010	B.S. in Mechanical Engineering, University of California, San Diego

Peer Reviewed Publications

1. **M. Garcia**, S. Pennathur, Modeling of inertial particle dynamics in curvilinear microchannels (submitted).
2. **M. Garcia**, R. Khojah, D. Di Carlo and S. Pennathur, Inertial focusing and enrichment of rare cells using μ-TFF (in preparation).
3. **M. Garcia**, B. Ganapathysubramanian, S. Pennathur, A linearised model for calculating inertial forces on a particle in the presence of a permeate flow, *Journal of Fluid Mechanics*, accepted (2018).
4. **M. Garcia**, S. Pennathur, Inertial Particle Dynamics in the Presence of a Secondary Flow, *Physical Review Fluids* **2**, 042201 (2017)
5. M. Brust, C. Schaefer, L. Pan, **M. Garcia**, P.E. Arratia, and C. Wagner, Rheology of human blood plasma: Viscoelastic versus Newtonian behavior, *Physical Review Letters*. **110** 078305 (2013)
6. N.C. Keim, **M. Garcia**, P.E. Arratia, Fluid elasticity can enable propulsion at low Reynolds number. *Physics of Fluids*, **24** 081703 (2012)

Conference Proceedings

1. **M. Garcia**, R. Khojah, D. Di Carlo and S. Pennathur Inertial focusing and enrichment of white blood cells using micro-tangential flow filtration. *Miniaturized Systems for Chemistry and Life Sciences*, (2017)
2. **M. Garcia** and S. Pennathur, In-situ particle control using inertial microfluidics combined with tangential flow filtration. *Miniaturized Systems for Chemistry and Life Sciences*, (2016)

Awards

1. Graduate Division Fellowship, University of California Santa Barbara (2014 & 2018)
2. 2nd place poster, SoCal Micro and Nano Symposium (2018)
3. The Tony B. Award, Society for Laboratory Automation and Screening (2017)
4. Mechanical Engineering Department Excellence Fellowship,University of California Santa Barbara (2014)
5. William Fontaine Fellowship, University of Pennsylvania (2010–2012)

Experience

2014–2018	Graduate Research Assistant, University of California, Santa Barbara.
2013	Summer Intern, ExxonMobil Research and Engineering
2010–2013	Graduate Research Assistant, University of Pennsylvania
2006–2009	Intern, Northrop Grumman

Abstract

Particle Migration and Focusing in Inertial Microfluidic Flows

by

Mike Garcia

The behavior of confined particles in microchannels at moderate Reynolds number has received much attention in recent years and has developed into a new area of research named "inertial microfluidics". This interest has been motivated by the development of high-throughput tools for the manipulation of bioparticles as a precursor for bio-analytic assays. However, a crucial first step towards developing these tools is understanding how particles are transported and localized in confined channels. Here I discuss how the interplay between axial and lateral flow in both a porous and curved microchannel results in non-trivial lateral migration and focusing of finite sized particles. To understand this behavior, I numerically explore this interplay by computing the lateral forces on a neutrally buoyant spherical particle that is subject to both inertial and secondary forces over a range of experimentally relevant particle sizes and channel Reynolds numbers. Interestingly, the lateral forces on the particles in both cases are well represented across a wide range of flow configurations using a simple perturbation based model. The representation of forces in this manner significantly reduces the complexity and time required to predict the migration of inertial particles in microfluidic channels. Finally, I experimentally validate this model and demonstrate how these moderate Reynolds number flows can be used to selectively enrich rare cells in a heterogeneous suspension.

Contents

List of Figures

Chapter 1

Introduction

1.1 Motivation

The ability to separate, sort and isolate particles is critical in a variety of bio-analytical applications including diagnostics, therapeutics, and fundamental biological studies and require exquisite cellular manipulations. Samples of interest are often just one specific cell type within in a large heterogeneous population of cells suspended in fluid; thus the isolation of any particular cell type is often a challenge. Many conventional and well established techniques have been developed for cellular isolation such as fluorescent activated cell sorting (FACS) [5], density gradient centrifugation [6], and selective cell lysis [7]. However, these techniques are often labor intensive and require large sample volumes with costly reagents, which may be suitable for a large clinical lab, but are still be too costly for widespread deployment.

Recently, there has been much interest in developing cost effective and simple techniques for manipulating particles of interest [8]. These techniques take advantage of microfluidic technologies and the intrinsic properties of target analytes such as size, shape, density, stiffness to make simple and relatively inexpensive tools. Generally the microfluidic technologies for particle manipulations can be classified into two categories i) active techniques, which take advantage of external fields and ii) passive techniques, which only utilize the interaction between particles, flow field and channel structure. Active techniques are often more versatile and better suited for targeting particles based their in-

trinsic properties than passive techniques. Unfortunately, they are also more complicated and expensive to fabricate due to the need for an external field. However, the performance of passive techniques is comparable to active techniques when the manipulating particles based on their size.

1.2 Passive size based particle separation techniques

Passive systems consist of a variety of methods that do not rely on any labeling of the target analyte. Instead, these methods rely on the differences in particle/cellular morphology to hydro-dynamically sort them. Given the simplicity of passive techniques, it is no surprise then that much work has been dedicated towards developing novel strategies for sorting and separating particles based on their size. These passive strategies include both low and high Reynolds number approaches.

Some common low Reynolds number approaches include microfluidic based filtration [9], pinched flow fractionation (PFF) [10], dynamic lateral displacement (DLD) [11]. Typically, these low Reynolds number approaches rely upon the particles directly interacting with structures along a channel to cause a size dependent shift in the particle's trajectory. For example, in the case of DLD, posts within a channel are arranged in a specific array to precisely control the trajectory of particles larger and smaller than a critical diameter. There are numerous reviews comparing and contrasting these methods [12, 9, 13]. In general, due to the linear nature of low Reynolds number flows these separation techniques are robust, easy to optimize and have proven successful for many applications. However, low Reynolds number flows are typically slow and thus their throughput is also low, which has prevented their widespread use and application in clinical settings.

High Reynolds number approaches leverage the phenomena of inertial migration and focusing and is commonly referred to as inertial microfluidics. Typically, these separation

modalities take advantage of the nonlinear fluid flow to discriminate particles based on their size/inertia. Inertial microfluidics has gained considerable attention since its first application in microfluidics by Di Carlo *et al.* [14], as it offers precise control of particles through the use of purely hydrodynamic interactions at high speeds. Since then there have been numerous reviews describing this technique in various transformative applications [15, 16, 17]. Unlike the low Reynolds number approaches highlighted previously, these set of techniques have a very high throughput $\mathcal{O}(10$ mL/hr). It is becoming increasingly clear that due to the robust, fault-tolerant physical effects employed and high rates of operation, inertial microfluidics is well positioned to have a significant impact on high-throughput separation in diagnostics and other fields. However, even with the benefits of this technique there are still questions that must be answered before widespread use is a reality.

This thesis attempts to answer some of these questions, namely:

i) Are there passive inertial techniques that allow for *in-situ* particle manipulations? Typically, inertial microfluidic techniques rely on the deterministic nature of particle focusing and thus devices can only be designed for one specific application. However, the ability to tune separations can prove useful in applications where the target analyte is not known *a priori*. The solution to this problem may well lie within a ubiquitous fluid system referred to as tangential-flow filtration (TFF). Using TFF in combination with inertial particle migration can control the particle dynamics in real-time and can be tuned for a multitude of applications.

ii) Are there ways reduce the complexity of modeling particle motion in these nonlinear inertial systems? Currently, inertial microfludics is increasingly being exploited in many fields, but there are few computational tools to easily design these devices. While many numerical simulations exist, the computational time often exceeds the time needed to build and test a device experimentally. Researchers desire

tools to accurately and rapidly predict the forces on particles in these nonlinear flows. To answer this question I examine the nature of these forces and reduce them down to their constituent parts.

1.3 Thesis structure

In this dissertation, I develop and model a novel technique to manipulate particle dynamics in real-time. The dissertation is organized into five parts:

Chapter 2: Details a novel inertial microfluidic device (termed μ-TFF) that can be used to focus particles *in-situ* into sized dependent streams. Here I also discuss how the interplay between axial and permeate flow in a porous microchannel results in non-trivial lateral migration of these finite sized particles.

Chapter 3: Presents an application of the μ-TFF device, where cells are manipulated and concentrated at a clinically relevant throughput.

Chapter 4: I develop a numerical model for the inertial lift force on a single particle in a square channel. While this has been extensively studied both analytically and numerically, I extend this model to include the effects of a permeate flow. I numerically explore the interplay between permeate and inertial forces on a neutrally buoyant spherical particle over a range of experimentally relevant particle sizes and channel Reynolds numbers. Interestingly, the lateral forces on the particle are well represented using a linearized model across a range of permeate-to-axial flow rate ratios. Finally, I experimentally validate this model for a range of flow conditions.

Chapter 5: I extend the principles of the model discussed in Chapter 4 and apply them to flow in a curvilinear channel. I compare and contrast my model with an existing linear model and a direct numerical simulation.

Chapter 6: I discuss the state of inertial microfludics and conclude my findings.

Chapter 2

Inertial particle dynamics in the presence of a secondary flow

2.1 Abstract

The manipulation of particles using inertial lift forces has broad implications in the separation, concentration and sorting of particles. In this work, we show that in the presence of a secondary flow, equilibrium locations of particles subject to inertial lift can be spatially varying. Using a well-defined microfabricated straight microfluidic channel with perpendicular permeate channels, we perform experiments over a range of particle sizes and inlet and outlet flow rates to highlight different focusing regimes. We show that a permeate flow can control the equilibrium location of particles and can be used to interrogate the balance between inertial and permeate forces.

2.2 Background

Migration and focussing of particles in finite Reynolds number flow is a phenomenon that has recently received a great deal of attention due to its ability to precisely manipulate cell and other biomolecules. Segre and Silberberg [18] experimentally documented this phenomenon in 1961, coined the "tubular pinch effect". Through their experiments in a circular pipe, they found that rigid particles migrated to an equilibrium position

shaped as an annulus, with a radius of about 0.6 times the pipe radius. Influenced by these experiments, many researchers have since developed analytic and numerical models to understand the physics governing migration in such flows [19, 20, 21, 1, 22], and have found that hydrodynamic inertial stresses can cause particles to laterally migrate across streamlines and ultimately focus into distinct locations in the channel (largely determined by the confining geometry of the channel) [1]. The competing forces include a wall lift force, a result of interactions between the particle and a confining wall acting to push the particle away from the wall, and a shear gradient inertial force caused by the gradient of the fluid velocity profile, pushing particles toward the wall. The balance between these two forces predicts the existence of an unstable equilibrium position at the centerline, and stable equilibrium positions somewhere between the channel centerline and the wall [19].

More recently, inertial migration techniques have been exploited in microfluidic systems for applications such as the separation [23, 24, 25], concentration [26] and sorting [27] of cells and biomolecules. In these studies, researchers rely exclusively on the deterministic nature of inertial focusing combined with the incorporation of clever geometric designs to manipulate analytes of interest. To date, no one has attempted to exploit permeate flows to dynamically control bioanalytes in inertial microscale fluidic systems, even though the incorporation of such flows is ubiquitous at the macroscale. For example, it has been documented that filtration efficiency is improved in hollow fiber membrane systems (*i.e.*, tangential flow filtration (TFF) systems) due to inertial lift forces facilitating the transport of microparticles away from membrane walls (thereby reducing fouling) [28, 29]. Predictive models of mass transfer in such filtration modules are largely based on simulating the single phase flow field in the channel and coupling the solution of the flow field to the solute mass transfer balance through the convective-diffusion equation [29]. Unfortunately, researchers often apply many simplifying assumptions with regards

to the hydrodynamic inertial effects on suspended particulates that either do not account for a spatially varying axial flow rates or the influence of a secondary flow on the underlying velocity profile [30, 31, 32]. For example, Altena and Belfort [32, 33] modeled and measured inertial particle motion in a porous duct to include the effect of a constant permeate force of a single wall on a particle. The theory calculated the trajectories of particles by assuming that the inertial contribution could be superimposed with the permeate forces, the applicability of which is limited to regimes of constant permeate flow and constant axial flow rates. Under typical operation of TFF, both permeate flow and axial flow rates are spatially varying due to the fouling of membrane walls and the presence of a permeate flow, respectively.

In this chapter, we fabricate well-defined square cross-section microfluidic TFF devices to study resulting particle equilibrium locations due to the interplay between permeate and inertial forces. we focus on a particular case of TFF where permeate flow is spatially dependent and interrogate how these permeate forces alter the behavior of particle equilibrium streams. By observing the particle equilibrium location for a variety of particle sizes, permeate and axial flow rates, we demonstrate a novel method for measuring the spatial variation of lift forces on a particle. Finally, we demonstrate the potential for particle separations by leveraging particle inertia in the presence of a permeate flow to shift particles into size dependent equilibrium streams.

2.3 Experimental Methods

Figure 2.1a shows a schematic of the microfluidic TFF device (μ-TFF). Both the primary and permeate channels are etched in silicon using typical microfabrication techniques, and anodically bonded to a transparent borosilicate wafer to prevent any swelling and delamination of the permeate channels under high operating pressures (figure 2.1b).

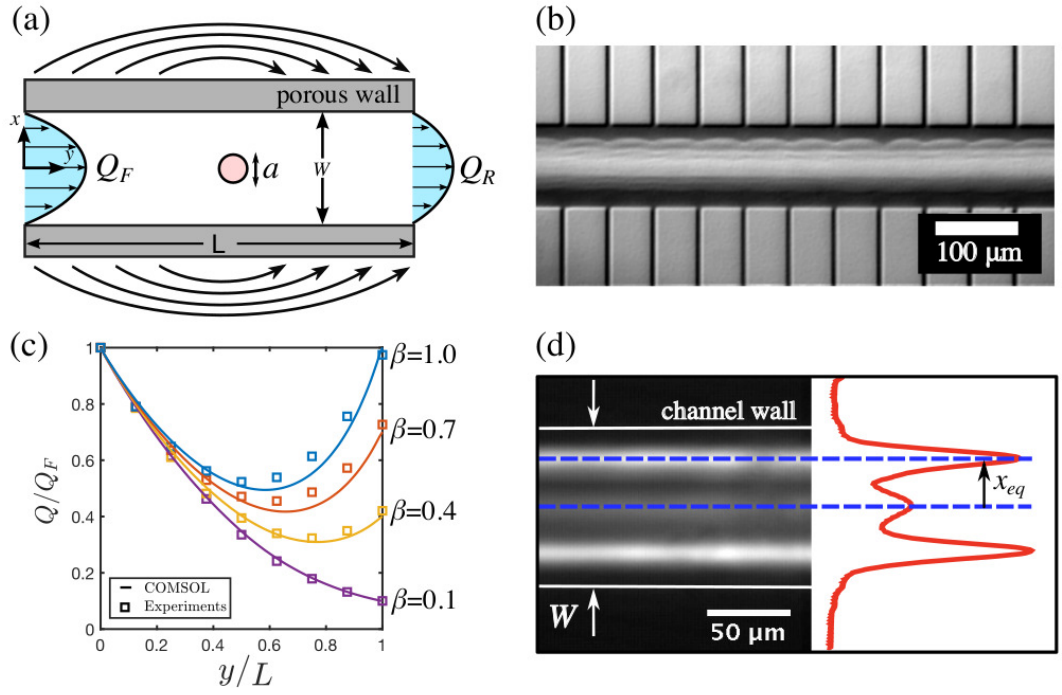

Figure 2.1: (a) Schematic of TFF device with recirculating flow (b) Image of the primary channel and several perpendicular permeate channels within a microfabricated TFF device (global view of the device can be seen in SI 1) (c) Non-dimensional flow rates versus channel length for varying β ($\beta = Q_R/Q_F$ = outflow/inflow). In each case, there is good agreement between COMSOL models and data. (d) (left) Long exposure image of 10 μm fluorescent polystyrene particles in a 100 x 100 μm TFF channel flowing at $Re = 83$. The in-plane particles equilibrate at a distance (x_{eq}) relative to the centerline. (right) Intensity distribution of the same image showing the intensity peaks used to determine (x_{eq}). Note that there are three peaks, the two larger peaks correspond to the equilibrium location of particles in-plane and the smaller peak is attributed to the out-of-plane equilibrium location of the flowing particles.

Briefly, photoresist (AZ 4620) is patterned on a 4-inch silicon wafer (100) through a single mask photolithography process, and subsequently etched using a standard Bosch process (Plasma-Therm 770 SLR) to create the high aspect ratios (AR = 20) of the permeate channels. The wafer is drilled to provide inlet and outlet vias using a 3-axis CNC drill (Flashcut),then bonded and diced (ADT100) into individual dies. The primary channel is 3.2 cm long with a square cross sectional area of 100 x 100 μm. Perpendicular to a 2.5 cm section of the primary channel are permeate channels of 5 μm width spaced

52.5 μm apart, with an average length of 415 μm (figure 2.1b & figure A.1). A two syringe pump system (Harvard Apparatus) modulates the permeate flow rate. The first pump infuses the inlet (feed) flow into the primary channel at a constant volumetric flow rate (Q_F). The second pump limits the outlet (retentate) flow rate from the primary channel by withdrawing fluid from the channel at a constant volumetric flow rate (Q_R). A global view of the device, outlining how the transverse permeate channels are arranged and how the permeate flow reaches the permeate outlets is provided in the appendix A.1 (figure A.1).

To perform experiments, we suspended three different fluorescent polystyrene particles (Sphereotech and FluoSpheres, 5.6, 10 and 15 μm) in DI water at a concentration of 10^4 particles/mL and add 0.5% v/v Tween 20 (Sigma-Aldrich) to reduce particle aggregation. Additionally, to measure the flow rates within the system, we conducted flow visualization experiments with 2.02 μm fluorescent polystyrene microspheres (Spherotech). We visualized all experiments with an inverted optical microscope (Olympus IX71) and mercury arc lamp illumination with the appropriate filter cubes (Chroma, Inc.). To find the particle equilibrium locations, we recorded streak images with a CCD camera (Andor Luca) by accumulating approximately 25 seconds of image data at each downstream location and post-processing using image processing software (MATLAB). Figure 2.1d shows an example of a streak image and the resulting post-processed data. Finally, we located the intensity peaks through a peak finding routine and determine particle stream position at various locations along the channel.

2.4 μ-TFF Design

Under typical operation, the TFF device diverts a portion of the flow in the primary channel through the permeate walls, and the flow is highly dependent on the device geom-

etry (appendix A.7). In this particular geometry, the permeate resistance is comparable to the main channel resistance thus the flow recirculates, *i.e.*, exits the channel upstream and reenters further downstream (figure 2.1a and 2.1c). To understand this global flow in our system, We developed a CFD model (COMSOL) of our device (figure 2.1c) where we specified the flow rates at the inlet of the channel and at the outlet of the channel, Q_F and Q_R, respectively, and $\beta = Q_R/Q_F$ is the non-dimensional parameter quantifying the global permeate flow. We determined the volumetric flow rate in the primary channel by modeling the system as an open boundary with no normal stresses, and acquired flow rates along the channel as shown in figure 2.1c. We experimentally validated this model through particle tracking velocimetry (figure 2.1c) for various values of β, and as expected, we observe a deviation from linearity of Q/Q_F due to recirculation. This design allows us to vary the permeate flow by simply tuning the flow rate ratio (β) which ultimately modifies the spatially varying permeate velocity and affects the migration of particles.

2.5 Results

Figure 2.2 shows a representative case ($a/W = 0.15$, $Re = 138$, $\beta = 1.0$) of the particle intensity distribution along the channel length (y/L) in the presence of a spatial varying permeate flow. The channel Reynolds number is defined by $Re = \rho UW/\mu$, where ρ is the density and μ is the viscosity of water, $W = 100\,\mu$m is the width of the TFF channel, and $U = Q_F/W^2$ is the mean inlet fluid velocity in the channel. We observe three distinct regions of particle positioning: (1) The channel entrance ($0 < y/L < 0.1$), (2) the outward permeate flow region, where the permeate flow is directed into the wall, and (3) the inward permeate flow region where the permeate flow is directed into the channel. At the entrance of the channel (1), the particles enter randomly dispersed since neither

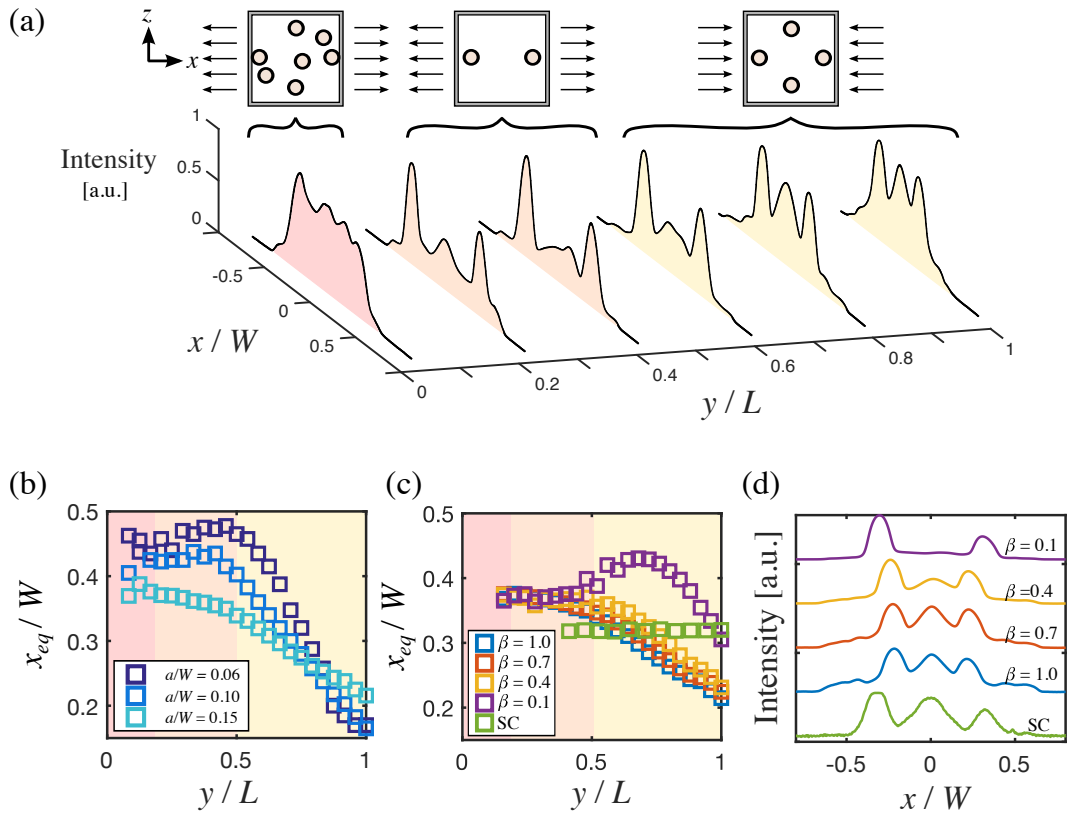

Figure 2.2: Experimental particle equilibrium locations in a TFF channel. (a) One experiment showing the distribution of particles along the length of the channel (y/L) and (top) a corresponding schematic illustrating the influence of permeate flow direction on cross-sectional distribution of particles. At the entrance (left), the particles are dispersed and unfocused. In the outward permeate flow region, the particles are moving towards the wall, and so the equilibrium position is closer to the wall, and the out-of-plane equilibrium positions are unstable. In the inward permeate flow region, the equilibrium position shifts away from the wall, due to the fluid from the permeate channels flowing into the main channel, and the out-of-plane equilibrium positions regain stability. (b) Streamwise equilibrium positions for the three different particle sizes, all at a Reynolds number of 138 and a β of 1.0. (c) Experiments showing the effect of β at a Re of 138 and a/W of 0.15. This graph also superimposes results from a straight channel device (SC) where the equilibrium position is constant throughout the channel. (d) Particle intensity distributions at the end of the channel ($y/L = 1$) for different β and a $Re = 138$. Here we see that as β decreases the out-of-plane equilibrium point disappears because more flow is diverted towards the wall, even at the end of the channel.

the inertial nor permeate forces have had significant time to influence the particles. This stage is characterized by poor focusing quality, as the particle intensity distribution has no clear peaks. Within the outward permeate flow region (2), the permeate flow out of the primary channel shifts the equilibrium positions of the in plane particles closer to the walls and simultaneously destabilizes the out-of-plane equilibrium positions. As a consequence, the two stable in-plane equilibrium locations contain the majority of the particles. Additionally, in this region the equilibrium locations of the particles are independent of β and channel location (y/L) (figure 2.2c), since the permeate flow at least in the first third of the channel is also nearly independent of β and y/L (figure 2.1c). The inward permeate flow region (3), beginning where the permeate flow is directed into the channel and ending at the outlet of the channel ($y/L = 1$), is the region where equilibrium locations along the permeate wall move towards the centerline, and are spatially-varying throughout the remaining length of channel. This is contrasted by the case of flow in a straight channel (SC) with no permeate channels (figure 2.2c, green), where the equilibrium positions are constant throughout the channel. Furthermore, the out of plane equilibrium positions become more prominent as y/L increases. This is because the inward permeate forces act to stabilize these positions, and since this occurs over finite time the repopulation of particles into the out-of-plane equilibrium positions transpires over some finite distance. Decreasing β shifts the location of the beginning of this region further downstream (this location being the extremum point of the lines in figure 2.1c) and allows less distance for the repopulation of the stable equilibrium to occur. This is evidenced by (figure 2.2d) where the prominence of the out of plane equilibrium decreases with decreasing β.

2.6 Discussion

The migration of equilibrium position in the third region is a direct result of the varying permeate flow acting away from the wall. To understand in more detail how permeate flow affects this migration, we examine the particle trajectories in region 3 (inward flowing permeate). We define transverse migration velocity as $U_m = dx_{eq}/dy \cdot dy/dt$, and where dx_{eq}/dy is calculated by using a linear fit of the measured trajectories (figure 2.3a), and the timescale dt is found by relating $U_{outlet} = dy/dt$ to the outlet stream-wise velocity $U_{outlet} = \beta Q_F/W^2$. Resulting migration velocities are shown to scale linearly with an effective Reynolds number $Re\beta$ (figure 2.3), suggesting that the migration we observe is largely a viscous phenomenon, unlike inertial migration (scaled as U^2)[34]. Although this migration is at least an order of magnitude slower than inertial migration, it is shown in figure 2.4a & b that the resulting equilibrium positions still depend on particle size. If viscous forces were the only force to balance the particle drag force, the resulting migration velocities should be independent of particle size (since both forces scale as a). We note that larger particles migrate slower, presumably because they are less susceptible to permeate forces since inertia scales as $F_L \sim a^4$. Therefore, permeate forces seem to dominate the migration of the particles, but fluid inertia is still extremely important in characterizing the equilibrium position of particles in TFF flow.

To gain further insight on the effects of permeate flow on the focusing behavior of the particles, in figure 2.4c we map β to the corresponding local permeate velocity (U_W). Specifically, figure 2.4c shows the difference in equilibrium location between a TFF and a SC for the same flow rate (βQ_F) as a function of the local permeate velocity at $y/L = 1$. As the magnitude of permeate velocity increases, the particles deviate further from the SC focusing behavior. Again, smaller particles deviate further than larger particles, but interestingly, all particles seem to match the SC focusing position when the permeate

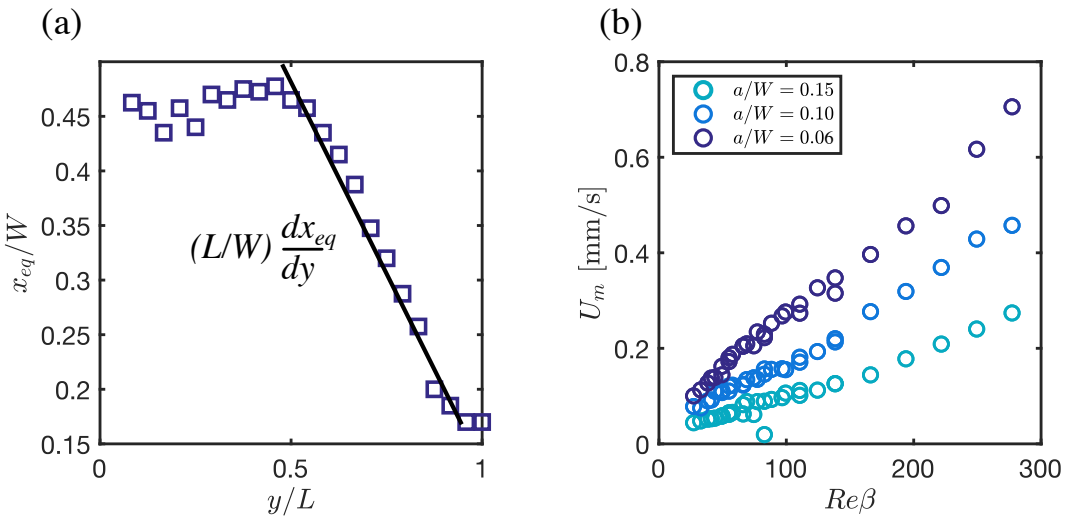

Figure 2.3: (a) Representative particle trajectory with fitted linear slope (b) Transverse migration velocities plotted against Reβ. The linear results indicate that the migration is largely dominated by viscous forces, however inertial aspects are apparently important since there is a dependence on particle size (*i.e.* data does not collapse).

velocity (U_W) is zero. Note that we experimentally find equilibrium locations for a SC (100 x 100 μm) as a function of Reynolds number (figure A.2), and interpolate between these values to generate the data in Figure 2.4C.

The TFF system also allows us to measure the forces on particles in a manner that is not compromised at higher particle velocity. In the past, the lift forces on particles flowing in a microchannel have been difficult to measure, particularly, in a manner that can capture the spatial distribution of the forces. Most recently, K. Hood *et al.* [34] calculated inertial forces by tracking individual particles and calculating their lateral migration velocities. While this technique has shown excellent agreement with theory [22], it is unclear that it would work as well for higher particles velocities, due limitations of image acquisition speeds. However, we can measure the forces on particles in a manner that is not altered by particle velocity (or equivalently Re), simply by taking advantage of a known permeate flow and how it perturbs an inertially focused equilibrium particle stream.

The lift forces on a given particle can be characterized by the lift coefficient (C_L), which is in general a function of Re and is spatially in-homogeneous [1, 35]. To calculate C_L we can compare the inertial and permeate forces at a given equilibrium location (x_{eq}) by constructing a simple model that linearly superimposes the permeate and inertial forces. The results shown in figure A.3 show that permeate flow perturbations do not have a significant effect on axial flow profile, supporting a superposition in such a manner.

$$3\pi\mu a U_m = F_P + F_L \tag{2.1}$$

Furthermore, we can relate the permeate flow to a resulting transverse force using Stokes drag $F_P = 3\pi\mu a U_W$ and the inertial forces to $F_L = C_L\rho(\beta U)^2\frac{a^4}{W^2}$ [21]. Finally, if we assume that the migration velocity is small compared to the permeate velocity at the outlet ($U_m/U_W < 0.1$) then we can derive a relationship for the inertial lift coefficient.

$$C_L = \frac{-3\pi\mu a U_W}{\rho(\beta U)^2\frac{a^4}{W^2}} \tag{2.2}$$

Figures 2.4d and 2.4e show our experimental data recast to plot exit equilibrium locations vs. calculated lift coefficient for varying inlet Reynolds numbers and particle sizes, respectively. The measured lift coefficient values are negative near the channel walls (wall lift dominance), positive near the centerline (shear gradient lift dominance), and also show a stable equilibrium that is shifted towards the wall for both decreasing particle size and increasing Re (note that Re is based on the inlet flow rate). Therefore, inertial lift coefficients determined by our system agree not only qualitatively, but also quantitatively with previous work [1, 35]. This technique can precisely measure the distribution of force near a particle in an inertial microfluidic flow in a manner that is not compromised at higher particle velocity. This may be useful for future measurements of inertial migration at even higher Re ($Re > 300$).

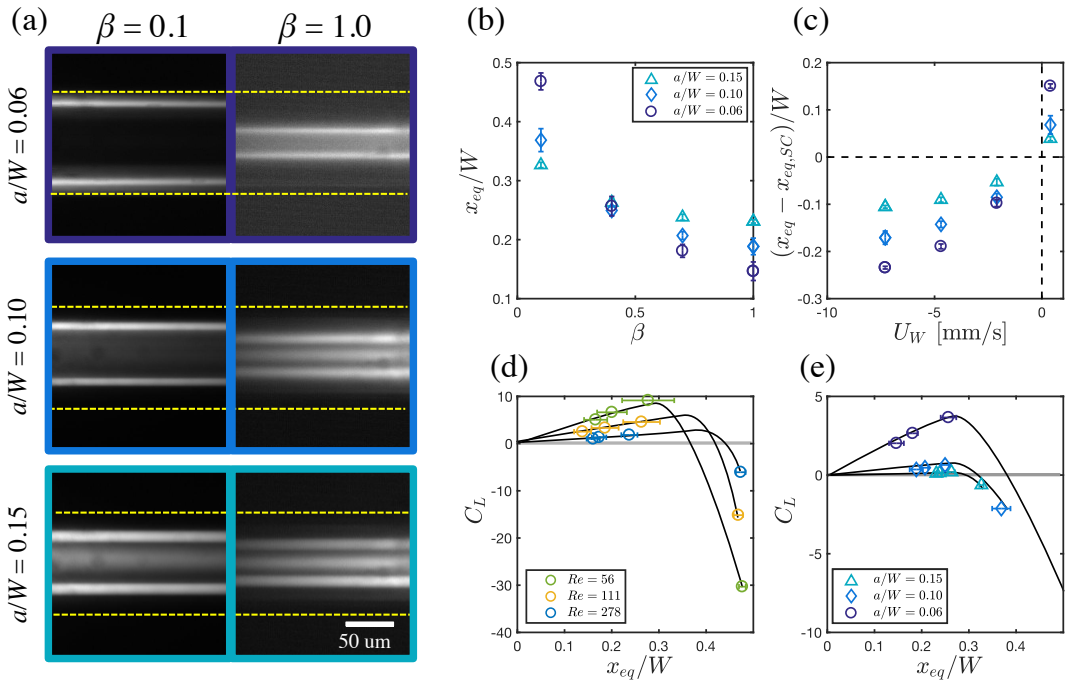

Figure 2.4: (a) Grayscale streaklines of the particle focusing with three different channel sizes and two values of β.(b) Endpoint equilibrium locations vs. β for three different particle sizes ($Q_F = 50\,\text{ml/hr}$ at $y/L = 1$). (c) The difference between measured equilibrium locations for a TFF channel and straight channel (SC) as a function of the local permeate velocity (U_W) at the wall for $Q_F = 50\,\text{ml/hr}$ at $y/L = 1$. The presence of a transverse permeate flow causes inertially focused particles to deviate from their SC equilibrium location. Smaller particles are more susceptible to permeate flow as characterized by larger deviations from the SC equilibrium for a given permeate flow. The location of the TFF equilibrium returns to that of the SC in the absence of permeate flow. Measured values of the lift coefficient (C_L) on particles flowing in a TFF channel for various (d) $Re = 56$, 11, & 278 $a/W = 0.06$ and (e) particle sizes $a = 5.6$, 10 and 15 μm ($Re = 138$).

Lastly, the TFF device is an excellent platform for particle separations because the location of the equilibrium streams is highly dependent on particle size, more so than its SC counterpart (figure A.2). This phenomena occurs because of the disproportionate effects of permeate forces on smaller particles compared to larger (figure 2.4c). figure 2.4b demonstrates that both β and particle size determine particle equilibrium position. Specifically, figure 2.4b shows particle equilibrium locations at $y/L = 1$ as a function of particle size and β. As expected, as particle size decreases, deviation in stream location

increases, and an increase in β focuses the particles closer to the centerline. While only a single Re ($Re = 138$) is highlighted in this figure, the trends are similar for lower Re (figure A.4). This is believed to be a consequence of the weak dependence of x_{eq} on Re ([21] and A.2). These data effectively show our ability to tune the location of a particle and/or separate different particles by simply modifying β.

2.7 Conclusion

The work presented in this chapter provides greater insight to the mechanisms influencing inertial migration and focusing in the presence of a secondary flow. The TFF system can not only dynamically manipulate the equilibrium location of particles, but also modify the state of equilibrium positions (stable vs. unstable). Using the TFF system we was able to measure the inertial lift forces acting on a particle by leveraging the distance an equilibrium stream is perturbed by an imposed permeate force. Finally, we demonstrated that the focusing position is strongly dependent on particle size. This enhancement can be attributed to increased susceptibility to permeate forces for smaller particles (see figure 2.4c). In particular, the optimal flow configuration tested seems to be at $\beta = 0.1$ where we observe a 3-fold increase in the separation distance between the SC counterpart. Thus, the insight gained through this fundamental study can be applied in the design of novel separation techniques, where *in-situ* manipulations of particles are needed.

Chapter 3

Inertial focusing and enrichment of rare cells using μ-TFF

3.1 Abstract

In the previous chapter we demonstrated that the combination of inertial focusing and a transverse permeate flow can enable precise and size based particle manipulation. Here we describe the use of the micro tangential flow filtration (-TFF) device for the simultaneous size based isolation and enrichment of circulating tumor cells (CTC). Specifically, in this chapter the we use the μ-TFF device, to demonstrate a proof of concept enrichment for rare cells (MDA-MB-231) at a throughput of 100 mL/hr. These results suggest that the μ-TFF device is a viable tool for separating, enriching and focusing cellular suspensions for downstream diagnostic and characterization applications.

3.2 Background

Circulating tumor cells (CTCs) are shed from a primary tumor and are carried through the blood circulatory system [36]. The isolation of these CTCs from the bloodstream offers a minimally invasive method to obtain cancer cells and can assist early patient prognoses, help determine individualized treatment and characterize treatment efficacy [36]. However, the difficulty in isolating CTCs is two fold: 1) They are rare,

occurring at concentrations on the order of 1 to 10 CTCs per mL of blood in patients with metastatic disease [36]. 2) They are dispersed among billions of red blood cells and millions of white blood cells. Thus isolating pure CTCs must address both issues and to date has proved a significant challenge.

There are many methods for isolating CTCs. However, the only FDA cleared blood test for enumerating and enriching CTCs is CellSearch ®. This system uses iron nanoparticles coated with anti-EpCAM antibodies for capturing and separating CTCs. Cells captured and magnetically manipulated, then fixed and fluorescently labeled to increase the sensitivity of the assay. The technique has many drawbacks including its high cost, need for specialized equipment and most significantly it renders the cells in-viable. Furthermore, this technology does not capture all types of CTCs, as capture is based upon the expression of EpCAM, and surface expression may vary significantly between patients.

Recently researchers have devised alternatives for capturing CTCs based on cell properties [37, 38, 39, 40]. E. Sollier and coworkers successfully combined the use of micro-scale vortices and inertial focusing, for the high-purity extraction of CTCs from blood samples [40]. This promising technique leverages the fact that CTC diameters for a range of cancer types are significantly larger than normal blood cells and thus captured in the micro vortices. However, this microfluidic approach and many others are typically done in a step-wise manner and are difficult to integrate into one continuous process, often requiring operator handling.

The approach outlined in this chapter makes use of the μ-TFF device to filter blood cells through the porous walls, while the larger CTCs are inertially focused and simultaneously concentrated in the feed channel. The entire process is passive and selectively enriches larger cells while smaller cells are flushed out of the device. First, we characterized the enrichment capabilities of the μ-TFF device using rigid polystyrene microspheres.

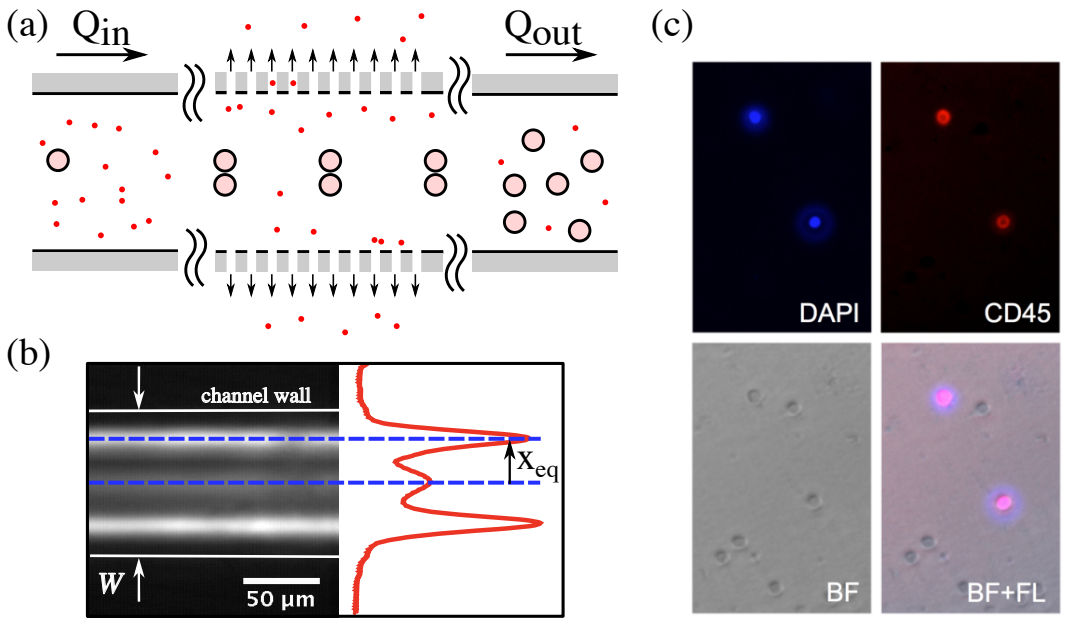

Figure 3.1: (a) Schematic illustration depicting the operation of the μ-TFF channel, where a suspension of blood cells enters at a rate of Q_{in} and exits at a rate Q_{out}. The permeate channels allow fluid flow and smaller particles to exit feed channel. (b) Fluorescent streak image showing the focusing behavior of inertial particles in the μ-TFF device showing the focusing location x_{eq}.(c) White blood cells stained with DAPI and anti-CD45-PE for fluorescent visualization and quantification.

Then, we validate the device using a suspension of CTCs in saline buffer. Finally, We demonstrate that blood cells are not enriched by the device under the same flow conditions in a continuous manner.

3.3 Experimental Methods

The experimental platform is described in greater detail in Chapter 2. Briefly, the μ-TFF device contains a microscale primary channel $L = 2.5\,cm$, $W = 100\,\mu m$ and an array of perpendicular permeate flow channels with a width of $W_p = 5\,\mu m$ and spaced $50\,\mu m$ apart. The channels are etched into silicon at a depth of $H = 100\,\mu m$ (figure 3.1a). The experimental setup consists of a two syringe pump system to modulate the permeate

flow at a constant volumetric flow rate. The first pump infuses the feed flow into the primary channel at a constant volumetric flow rate (Q_{in}). The second pump withdraws fluid from the channel at a constant volumetric flow rate (Q_{out}) (figure 3.1a); thus the global permeate flow is set by the difference of these two rates $Q_{perm} = Q_{in} - Q_{out}$. Finally, the experiments were all performed using a fixed volume of 5 mL per run.

Experiments were performed with fluorescent polystyrene microspheres at a dilute concentration ($\phi < 0.01\%$), and with blood cells that are diluted form whole blood in a phosphate buffered saline (PBS) solution. Experiments with CTCs were performed using MDA-MB-231 cells (MDA) at a concentration of 10^5 cells/mL and were conducted separately from blood experiments. The MDA-MB-231 cell line is an epithelial, human breast cancer cell line that is one of the most commonly used breast cancer cell lines in medical research. As before, fluorescent streak imaging was used determine the particle equilibrium location (x_{eq}) at the device outlet (figure 3.1b). The inlet and outlet concentration of the rigid particles, red blood cells (RBCs), white blood cells (WBCs) and MDA cells were measured with a hemocytometer (iNCYTO, DHC-N01). The concentration of white blood cells was determined using fluorescent imaging with an DAPI and anti-CD45 label (figure 3.1c).

3.4 Results and Discussion

The ability to concentrate particles in the μ-TFF device is inherent to its design. Concentration occurs when particles larger than the permeate channel width ($W_p = 5\,\mu m$) are retained in the primary channel while the suspending fluid containing smaller particles is diverted through the permeate channels. The number of large particles ($a > W_p$) flowing through the device is constant and thus we can derive an expression relating

the inlet to outlet concentration:

$$C_{in}Q_{in} = C_{out}Q_{out} \tag{3.1}$$

where C is the particle concentration and Q is the volumetric flow rate. Using equation 3.1 we can then predict the concentration factor at the outlet of the μ-TFF to be:

$$C_{out}/C_{in} = Q_{in}/Q_{out} = 1/\beta \tag{3.2}$$

The separation and concentration of large MDA cells relies on the combination of both inertial focusing and permeate flow. Under ideal operating conditions, the μ-TFF focuses smaller cells (RBCs and WBCs) near the channel wall and subsequently siphons them out through the permeate channels. The larger CTCs are left intact in a focused stream away from the walls of the channel and thus avoiding any clogging of the permeate channels (figure 3.1a). However, the addition of a permeate flow causes the particles to focus at size-dependent equilibrium locations where in general larger particles are focused near the wall (figure 3.2b). It is only when β is small that this relationship inverts and we see the optimal focusing configuration (figure 3.2a). For the flow rates tested (Q_{in} = 100 ml/hr, β = 0.1 to 1.0) we found that under the flow configuration of $\beta = Q_{out}/Q_{in} = 0.1$ MDA and WBC cells achieved significant equilibrium separation, where WBCs focused near the channel wall and MDA cells focused near the channel centerline (figure 3.2a). This result is qualitatively similar to the focusing of the rigid sphere counterparts; the difference being that the focusing location of the cells is shifted towards the centerline by $10\,\mu m$, which can be attributed to lift forces associated with cell deformability (figure 3.2b)[41, 42, 43].

Next we characterized the concentration capabilities of the μ-TFF device using rigid

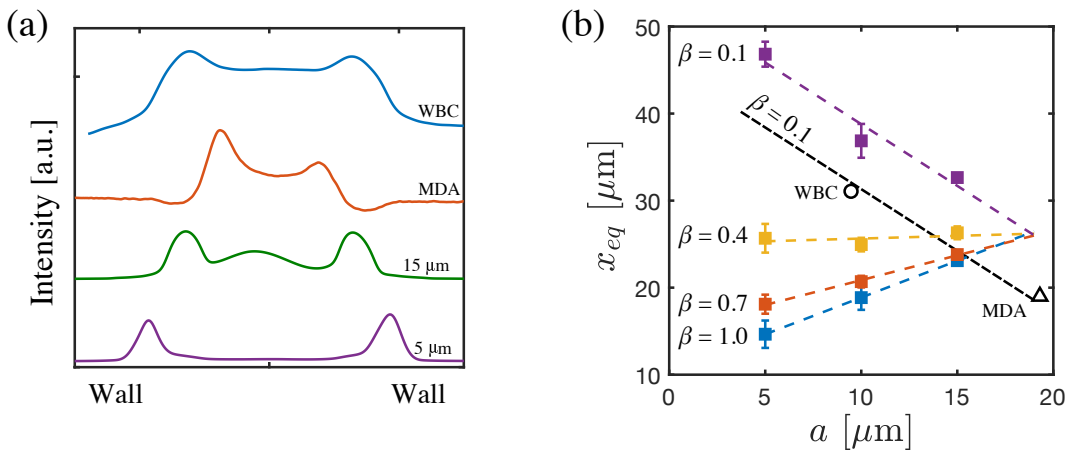

Figure 3.2: (a) Particle/cell distributions in the TFF channel for $\beta = 0.1$ and (Q_{in} = 100 ml/hr) as measured through fluorescent intensity streak images. White blood cells focus near wall and MDA cells focus near centerline. (b) Equilibrium focusing location (x_{eq}) as a function of particle diameter (a) for four flow configurations β. The black points and dashed line represent the focusing location of the deformable cells, measured at $\beta = 0.1$, which is offset by $10\,\mu m$ from the corresponding flow configuration of rigid particles (purple).

polystyrene particles at Q_{in} = 100 ml/hr. Under these conditions the polystyrene particles behaved as theoretically predicted (figure 3.3a and 3.3b). Where large particles ($a = 15\,\mu m$) were retained and concentrated by a factor of $1/\beta$ and small particles ($a = 2\,\mu m$) were not concentrated at all. Interestingly, the intermediate particle size ($a = 4.5\,\mu m$) did concentrate even though the size cutoff for concentration was $W_p = 5\,\mu m$, which may be attributed to hydrodynamic screening effects. Finally, we demonstrate the ability of μ-TFF device to concentrate RBCs ($a = 5.8 \pm 0.9\,\mu m$), MDA cells ($a = 19.3 \pm 4.6\,\mu m$) and WBCs ($a = 9.5 \pm 2.4\,\mu m$) (figure 3.3c). The highly deformable WBCs and RBCs do not concentrate even though their diameter is larger than the size cutoff. They are capable of deforming to a such a high extent that they are unhindered by the permeate channel. Conversely, the MDA cells which are also deformable, but much larger than the cutoff do concentrate. MDA cellls concentrate similarly to large rigid particles.

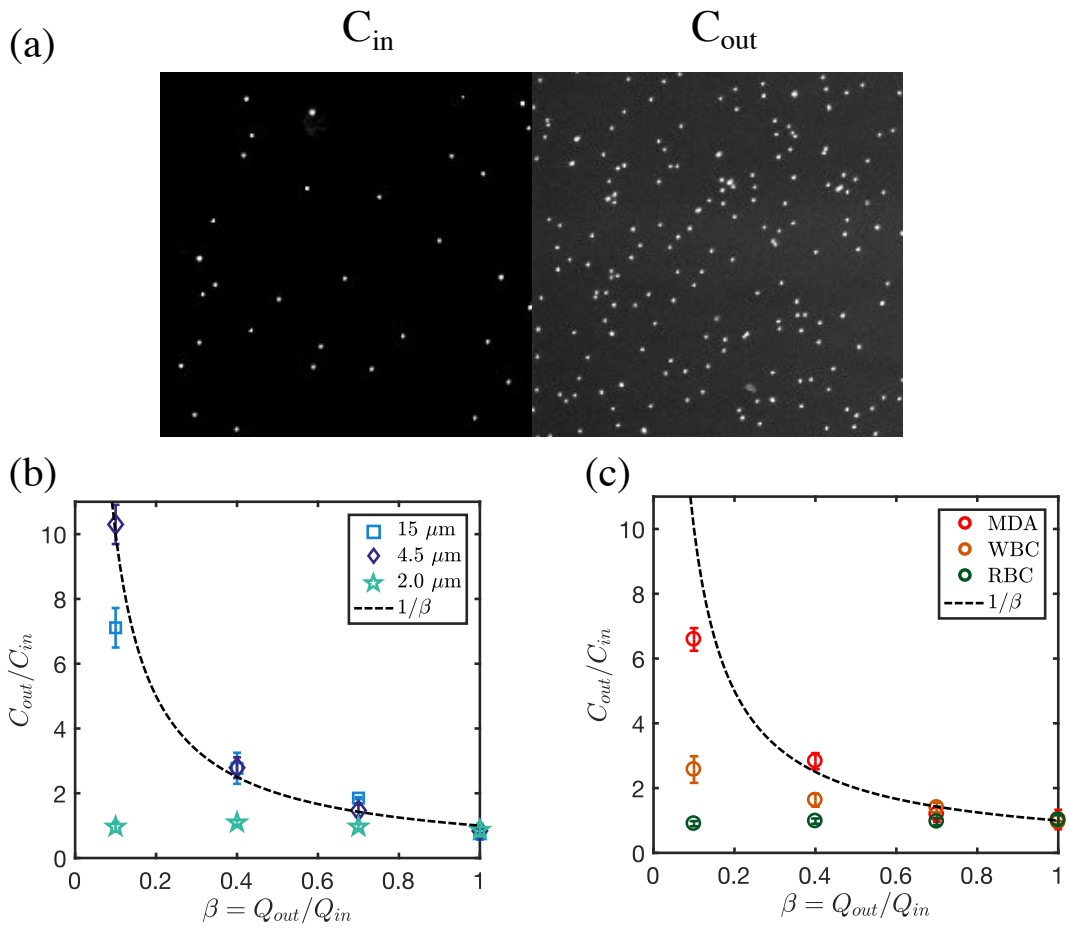

Figure 3.3: (a) Fluorescent images showing particles in a hemocytomer slideof fixed volume before and after concentration in μ-TFF device.(b) Concentration curve for rigid polystyrene particles. Large particles are retained and concentrated, but smaller particles are not.(c) Concentration curve for deformable cells. Large MDA cells are retained and concentrated, but smaller WBC and RBC are not.

3.5 Conclusion

This simple yet effective method for dynamically manipulating particle equilibrium locations in a microfluidic channel shows promise as a device capable of separating, enriching and focusing rare cells. Specifically, the work presented in this chapter shows that MDA cells were selectively concentrated by a factor of $1/\beta = Q_{in}/Q_{out}$ at the outlet of the μ-TFF, while RBCs and WBCs were not. This low volume study was a proof of concept and thus limited operation of the μ-TFF device to only $\beta = 0.1$. However, for

larger clinically relevant sample volumes, the μ-TFF can operate at much lower values of β and thus provide significantly higher concentrations. Furthermore, the performance of the μ-TFF can be enhanced by running several devices in series theoretically scaling concentration by $(1/\beta^n)$, where n is the number of devices. These preliminary results for pure CTC collection from artificial samples are the critical first steps developing a tool that may address an unmet clinical need. While, the device is promising more work needs to be done to understand the interplay between the flow parameters, channel geometry and cellular properties on effective sample enrichment.

Chapter 4

A linearized model for calculating inertial forces on a particle in the presence of a permeate flow

4.1 Abstract

Understanding particle transport and localization in porous channels, especially at moderate Reynolds numbers, is relevant for many applications ranging from water reclamation to biological studies. Recently, researchers experimentally demonstrated that the interplay between axial and permeate flow in a porous microchannel results in a wide range of focusing positions of finite sized particles [2](Chapter 2). Here we numerically explore this interplay by computing the lateral forces on a neutrally buoyant spherical particle that is subject to both inertial and permeate forces over a range of experimentally relevant particle sizes and channel Reynolds numbers (Re). Interestingly, we show that the lateral forces on the particle are well represented using a linearized model across a range of permeate-to-axial flow rate ratios, γ. Specifically, our model linearizes the effects of the permeate flow, which suggests that the interplay between axial and permeate flow on the lateral force on a particle can be represented as a superposition between the lateral (inertial) forces in pure axial flow and the viscous forces in pure permeate flow. We experimentally validate this observation for a range of flow conditions. The linearized

behaviour observed significantly reduces the complexity and time required to predict the migration of inertial particles in permeate channels.

4.2 Introduction

Lateral migration and focusing of neutrally buoyant solid particles at moderate Reynolds number (Re) in a confined pressure driven flow is a well known phenomenon first documented by Segré and Silberberg in 1961 [18]. Specifically, hydrodynamic inertial stresses cause particles to laterally migrate across streamlines and ultimately focus into distinct locations in the channel [19]. In addition to the seminal work on inertial migration and focusing [44, 19, 45] there have also been a few recent reviews highlighting progress [46, 47, 17]. However, comparatively, there have only been a few studies on the motion of inertial particles in the presence of a permeate flow. Systems with such flows are ubiquitous in applications related to pressure-driven membrane filtration for the separation of particles and cells from liquid suspensions as well as in a multitude of other areas, including wastewater treatment [48], food [49] and beverage [50] processing, and biotechnology [51, 52].

In general, to precisely solve for the forces on a particle in inertial migration problems, one relies on simulation of the combined fluid-particle interaction problem. For example, Chun and Ladd [53] used the lattice-Boltzmann method for Re ranging from 100 to 1000 to show that spherical particles migrate to one of a finite number of equilibrium locations in the cross-section of a non-porous square channel, where only the face centeredd equilibrium locations are stable for lower Re. Di Carlo *et al.* [1] performed simulations to show how particle equilibrium locations varies with particle sizes (a trend not captured by previous analytic approaches). Similarly, Liu *et al.* [54] performed exhaustive simulations to determine the non-trivial relationship between the focusing location of particles

and their size, channel aspect ratio, and Re. These numerical studies fit into generalized formulae and shed light on how the forces on a migrating particle are distributed within a channel and how this distribution depends on particle size. Such findings are crucial for practical device design.

With the addition of permeate flow, the interplay between the effects of axial and permeate flow (see figure 4.1a) results in a much richer particle behaviour than the case of pure inertial migration of a particle in axial flow [32, 55, 56]. Earlier theoretical work by Belfort and coworkers accounts for the effect of wall porosity on particle motion in a 2D geometry [32, 55] and has been validated experimentally [33]. In these theoretical studies, researchers employed asymptotic analysis to derive expressions for the forces on a migrating particle as a sum of inertially induced forces and permeate drag. While useful from a theoretical perspective, the researchers were unable to precisely predict the lateral lift forces of highly confined particles in a porous channel. This limitation is particularly critical since precise force values across the cross-section are required for efficient device design that exploit the lateral migration of particles to separate and concentrate particles with high specificity. More recently, Garcia and Pennathur [2] experimentally demonstrated that a permeate flow can drastically alter the migration and focusing of confined particles in inertial flow, with particle size significantly impacting resulting migration behaviour. However, no model to date has accurately described this behaviour. The ability to construct a simple model that reliably predicts these forces across a wide range of conditions serves as the overarching motivation for the present work.

Based on observations from a finite number of full-scale simulations, we develop a linear model to efficiently predict the lateral forces acting on a neutrally buoyant spherical particle migrating in a pressure driven porous channel. We first employ a previously utilized full-physics simulation approach [1, 57, 58, 22] to numerically simulate a spherical

particle translating in a square cross-section microchannel. We additionally validate this model against previously published work and experiments, then exploit the model to study the lateral forces in a system with permeate flow of varying magnitude and direction. We observe that the relative permeate flow, γ, can generalize the data over many particle sizes and Re, which provides a conceptual basis for developing a new linear model. We finally validate our linear model using the full-physics simulation, and determine that the limits of applicability are well within those of most experimental systems. To prove as much, we design a microfluidic system to experimentally validate the results of the linear model.

4.3 Full Physics simulations of particle-fluid interaction

The present work focuses on the combined inertial and permeate migration of a single neutrally buoyant spherical particle in Poiseuille flow within the confining geometry of a porous channel of square cross-section ($W \times W$) and length $L_C = 10W$. Here the particle of diameter a is translating with velocity $\mathbf{U}_P = [0, U_P, 0]$ and angular velocity $\mathbf{\Omega}$ in a flow of average (local) velocity $U = (U_{in} + U_{out})/2$, where U_{in} and U_{out} are the average axial flow velocities at the inlet and outlet of the porous domain respectively. The porous channel allows for a lateral flow to exist that emanates from only two parallel walls at a constant velocity U_W. Here the channel Reynolds number is defined as $Re = \rho UW/\mu$ and the relative permeate flow $\gamma = U_W/U$, where ρ and μ are the fluid density and viscosity respectively.

We consider a moving frame of reference translating with the accelerating particle [1].

[1] In this moving reference frame, the lateral flow extends a length $3W$ as depicted in figure 4-1

In this reference frame, we solve the steady Navier-Stokes equations:

$$\rho\big(\mathbf{u}\cdot\nabla\mathbf{u}+\mathbf{U}_P\cdot\nabla\bar{\mathbf{u}}\big)=\mu\nabla^2\mathbf{u}-\nabla p \tag{4.1}$$

$$\nabla\cdot\mathbf{u}=0 \tag{4.2}$$

where p is the fluid pressure, $\mathbf{u}$ is the fluid velocity in the reference frame of the translating particle and $\bar{\mathbf{u}}$ is the undisturbed flow. Note that the additional inertial term arises due to the acceleration of the chosen reference frame (appendix A.5).

The velocity of the suspended particle (U_P and $\mathbf{\Omega}$) can be self-consistently determined by setting conditions such that the axial motion satisfies a drag constraint $F_y=0$ (equation 4.3) and its rotational motion satisfies a torque constraint $\tau_x=\tau_y=\tau_z=0$ (equations 4.4). Justification for this assumption can be found in appendix A.8.

$$F_y\equiv\mathbf{e}_y\cdot\int_s\mathbf{n_r}\cdot\mathbf{T}\,ds=0 \tag{4.3}$$

$$\tau_i\equiv\mathbf{e}_i\cdot\int_s(\mathbf{r}-\mathbf{r}_p)\times\mathbf{n_r}\cdot\mathbf{T}\,ds=0\quad\text{where } i=x,y,z \tag{4.4}$$

where the integrals are over the surface of the sphere, $\mathbf{r}_p$ is the particle position vector that points from the center of the channel to the center of the particle and $\mathbf{n_r}=(\mathbf{r}-\mathbf{r}_p)/|\mathbf{r}-\mathbf{r}_p|$ is the unit normal at each point on the surface of the sphere. $\mathbf{T}$ is the total stress tensor and, for an incompressible Newtonian fluid, is given by $\mathbf{T}=-pI+2\mu\boldsymbol{E}$, where $\mathbf{E}=\frac{1}{2}(\nabla\mathbf{u}+\nabla\mathbf{u}^T)$ is the rate of strain tensor.

The boundary conditions of this problem are in the reference frame of the translating

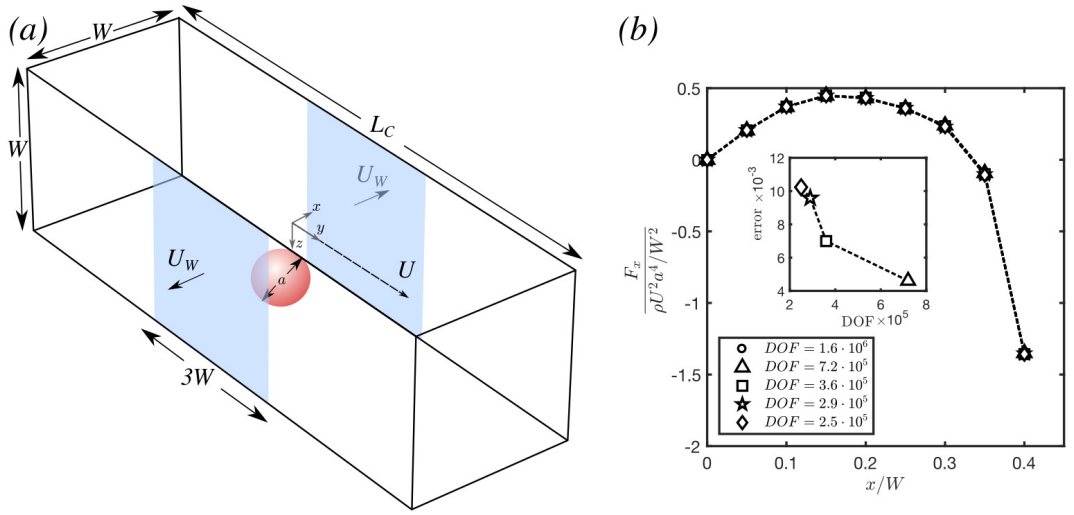

Figure 4.1: (a) Schematic illustration of the square channel model with average flow velocity U. In the channel a spherical particle of diameter a is migrating within the confines of the bounding walls where two of the walls are permeable (yz-plane) and allow flow to penetrate at a constant rate of U_W. For each $x-z$ location of the particle in the channel cross section, the lateral lift forces (F_z and F_x) are calculated. (b) Mesh sensitivity analysis showing that the calculated lift forces have converged and are, thus, insensitive to the degrees of freedom (DOF) in the model. The inset depicts the error relative to a model with 1.6×10^6 DOF. ($Re = 100$, $a/W = 0.1$).

particle. Therefore, the no slip condition on the wall is:

$$\mathbf{u} = -U_p \mathbf{e}_y \quad \text{on all walls} \tag{4.5}$$

additionally, the channel has two parallel porous walls that can advect fluid into or out of the channel at a constant rate of U_W. Thus the condition on these walls also must satisfy:

$$\mathbf{u} \cdot \mathbf{n} = U_W \tag{4.6}$$

where $\mathbf{n}$ is the wall unit normal pointing out of the channel and a positive value of U_W indicates flow out of the channel. The no slip condition on the rotating particle is enforced by assigning a velocity to the surface of the sphere corresponding to that of

rigid body rotation at angular velocity, $\mathbf{\Omega}$:

$$\mathbf{u}_{surface} = \mathbf{\Omega} \times (\mathbf{r} - \mathbf{r}_p) \tag{4.7}$$

Finally, far from the particle the flow field satisfies

$$\mathbf{u} = \bar{\mathbf{u}} - U_p \mathbf{e}_y \tag{4.8}$$

To solve for the unknowns (*i.e.* $\mathbf{u}$, p, U_p and $\mathbf{\Omega}$) we couple equation 4.3 and equation 4.4 to the fluid flow equations and solve directly using the COMSOL multiphysics software. This procedure is performed for a lattice of discrete positions of the particle within the cross-section of the channel (using only a quarter of the domain via symmetry arguments to minimize computational effort). To calculate the lift force on the particle, we integrate the surface stresses on the particle in the appropriate direction (x or z):

$$F_i = \mathbf{e}_i \cdot \int_s \mathbf{n}_r \cdot \mathbf{T}\, ds \quad \text{where } i = x, z \tag{4.9}$$

4.4 Numerical Results

4.4.1 Mesh convergence analysis

We discretize the fluid domain using tetrahedral elements in COMSOL Multiphysics. The surface of the sphere is discretized into triangular boundary elements (BE) with 6 boundary layer (BL) elements at the surface of the sphere to accommodate large gradients. We use quadratic basis functions for representing the velocity solution and linear basis functions for the pressure. The resulting discretization has approximately 3.6×10^5 degrees of freedom (DOF). To show that the calculated results were independent of mesh

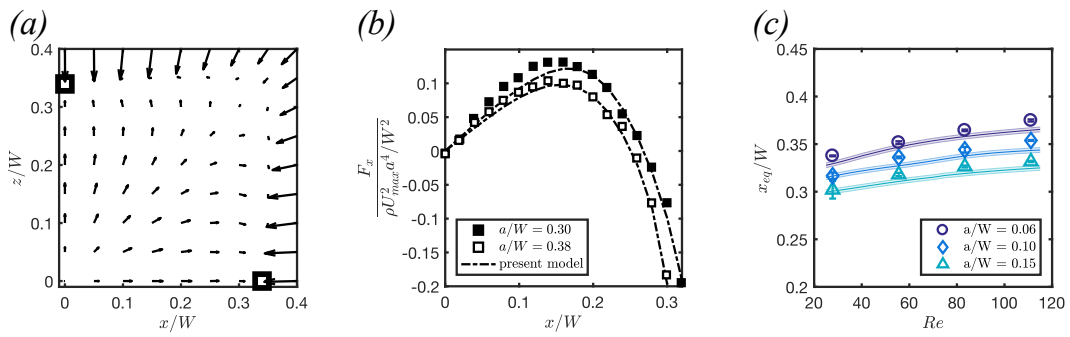

Figure 4.2: (a) Inertial forces calculated in a single quadrant of the square cross-section for a particle of $a/W = 0.10$ at $Re = 100$. Here the black small squares indicate the locations of the stable equilibrium points, *i.e.* locations where the lift forces go to zero. (b) A comparison of the x-component inertial forces along the $z/W = 0$ axis between the present study and that of Di Carlo *et al.* [1], showing good agreement at $Re = 38$ for two particles $a/W = 0.30$ and $a/W = 0.38$. (c) Experimental measurements (discrete points) from Garcia and Pennathur [2] of the inertial focusing locations (x_{eq}/W) as a function of Re for three particle sizes (a/W) with overlaid corresponding numerical simulations (solid lines).

density We increased the number of DOF in our model by varying the BE, BL and fluid domain tetrahedral density. The resulting calculated lift forces are shown in figure 4.1b, and show no significant differences ($\leq$ 1% change) in the spatial lift force among the different cases.

4.4.2 Model validation

To demonstrate validity of the model, we performed simulations of a particle within the channel with no permeate flow ($U_W = 0$), since this reduces to the well-studied case of an impermeable channel [1, 59, 60]. Typically in experimentally relevant flows for inertial microfluidic systems, particle diameters are a significant fraction of the channel width ($a/W \geq 0.10$) and generally Re ranges from $\sim$ 10 to 100. In the case of an impermeable channel under these conditions, particles focus to four symmetric equilibrium positions near the center of each wall face and approximately $0.3W$ away from the channel center [1]. Figure 4.2a provides a detailed map of the spatially varying inertial lift forces in a

single quadrant of a channel. With this map, we can identify the location of zero lateral lift force, which agrees with previous experimental studies [59, 60]. In figure 4.2b, we compare the spatial variation of the lift forces on the particle which show good agreement with data from Di Carlo *et al.* [1] (figure 4.2b). Finally, We show that the model can correctly predict changes in the locations of equilibrium with increasing Re [21] and increasing particle size [1] in figure 4.2c, where we compare our previous experimental data [2], with current simulation results.

4.4.3 Permeate flow results

We next consider the effects of permeate flow, for a range of Re, γ ($\gamma = U_W/U$), and particle sizes. We consider $Re = 25, 50, 75, 100$, $\gamma = \pm 0.003, \pm 0.002, \pm 0.001, 0$ and particle sizes $a/W = 0.05, 0.10, 0.15$. Figure 4.3a & b plots the lateral lift force vectors for a subset of the simulations. Figures 4.3c-h show the equilibrium locations for the full range of γ and Re, with figures 4.3a & 4.3b showing full force vector fields for the extreme cases. At large Reynolds number (Re) and large particle size (a/W), the vector fields are only slightly disturbed by the presence of the permeate flow when compared to the case with no permeate flow ($\gamma = 0$) (*e.g.* figure 4.3a), presumably because inertial lift forces are more dominant (since the lift force $F_L \sim a^4$ [21]). Conversely, for flows with less inertia (*i.e.* smaller Re and a/W) (*e.g.* figure 4.3b) the vector fields are highly disturbed due to the substantial effects of permeate flow. Specifically, for $\gamma = 0.003$ (*e.g.* figure 4.3b right), we observe a complete suction where the force equilibrium coincides with the location where wall contact occurs and is when all 'streamlines' appear to be guided towards the porous wall ($x/W = 0.5$)[2]. Conversely, when $\gamma = -0.003$ (*e.g.* figure 4.3b left), there is a reversal of 'streamlines', now directed towards the centerline

[2]We do not actually model the physics of wall contact, when referring to wall contact we do so in the context of the particle equilibrium location *i.e* $x_{eq}/W \geq 0.5 - a/2W$.

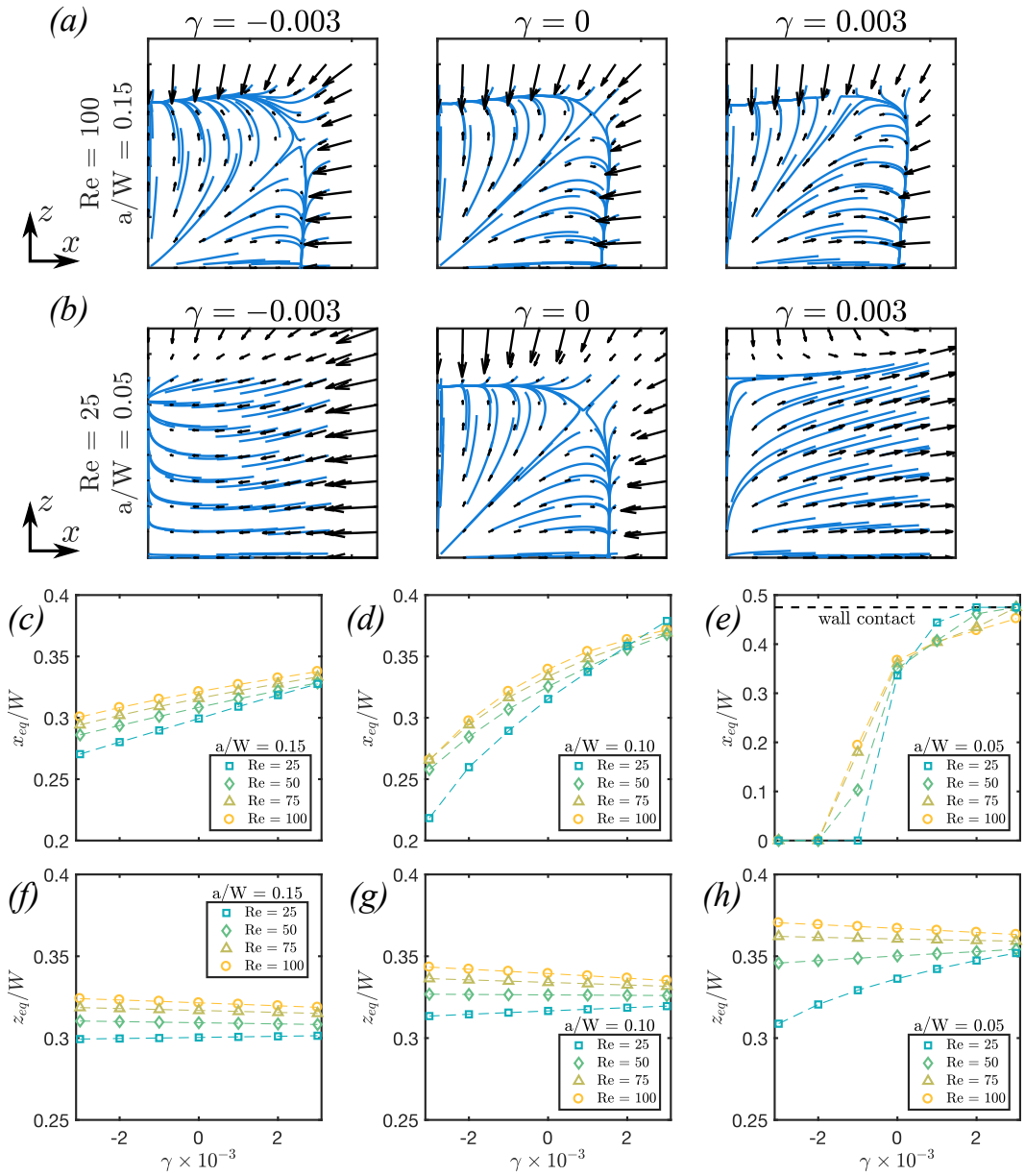

Figure 4.3: Lateral force vector fields spanning the extremities of the parameter space $\gamma = [-0.003 : 0.001 : 0.003]$ and $Re = [25 : 25 : 100]$ for two particle sizes (a) $a/W = 0.15$ (b) and $a/W = 0.05$. The blue 'streamlines' are for visualization of the vector fields which are bounded by a $0.45W \times 0.45W$ box. (c-e) x-equilibrium locations for all direct simulations in this study along the $z/W = 0$ axis for (c) $a/W = 0.15$ (d) $a/W = 0.10$ and (e) $a/W = 0.05$. Note that the equilibrium shift is in the direction of the permeate flow. (f-h) z-equilibrium locations for all direct simulations in this study along the $x/W = 0$ axis for (f) $a/W = 0.15$ (g) $a/W = 0.10$ and (h) $a/W = 0.05$.

$(x/W = 0)$.

Figures 4.3c-h captures all these observations as we plot the $x-$ and $z-$ force equilibrium location (x_{eq}/W and z_{eq}/W) for all Re and a/W. Through this representation we can clearly see that as permeate flow increases, the equilibrium location of each vector field shifts in the direction of the permeate flow (figures 4.3c-e). Furthermore, in agreement with the qualitative observation in figure 4.3a,b the shift in equilibrium location becomes less sensitive with increasing a/W and Re. We also see a slight shift in the z-equilibrium with the addition of a permeate flow, but in general the z-equilibrium shift is less sensitive than the x-equilibrium counterpart. One thing to note is that the z-equilibrium shifts either towards or away from the wall as a function of γ, depending on the flow Re. In general, there is a clear dependence on two factors, the first being the magnitude of permeate forces (set by U_W) and the second being the magnitude of inertial forces (set by U). The combination of these two factors dictates the behavior of the particles in our geometry, ultimately leading to non-trivial force fields.

4.4.4 Linearized Model

Solving for the effect of combined inertial and permeate forces with full-physics numerical simulations can quickly become computationally infeasible. For instance, the results in the previous sub-section involved performing $4(Re) \times 3(a/W) \times 9(x/W) \times 9(z/W) \times 7(\gamma) = 6804$ simulations, that required expending substantial computational resources. The computational requirements become even larger when modeling dynamic processes where a particle may be migrating in a continuously varying flow field, or in which γ is spatially and/or temporally changing. Therefore, we develop a linearized model (based on observations from the previous sub-section) to produce quantitatively similar results to the full simulation, but with significantly less computational requirements.

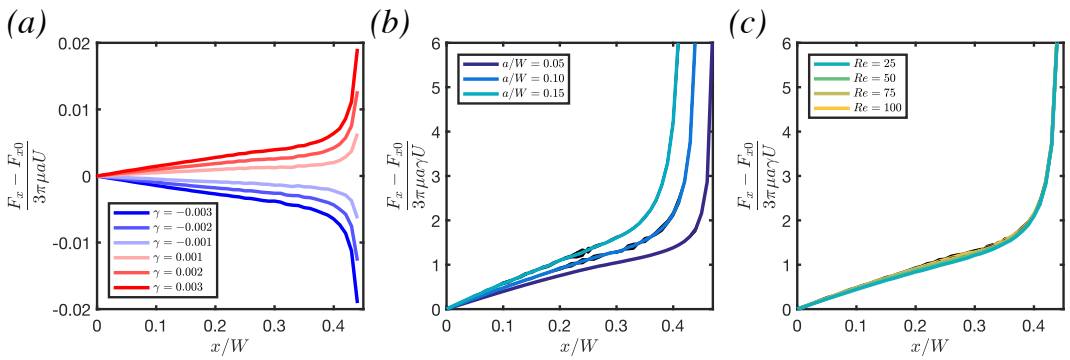

Figure 4.4: (a) Residual force plot. Each curve represents a different value of γ, where the residual is the difference in the force between a particle in the presence of permeate flow and a particle in a channel with no permeate flow ($\gamma = 0$) at different x locations. (b) The force residuals for all γ normalized by a characteristic drag force resulting in three distinct master curves corresponding to each particle size at $Re = 100$. (c) Normalized force residuals for four distinct Re at a constant particle size ($a/W = 0.10$). Note that normalizing in this manner results in the collapse of the curves into a single 'master curve'. Due to noise in our simulations, we averaged values in both (b) and (c) as shown in the colored lines. Black curves underneath represent the raw normalization).

We consider a linearization of the lateral lift force $\mathbf{F}(\gamma, Re, a/W, x/W, z/W)$ about the $\gamma = 0$, *i.e.* impermeable channel case. There are multiple reasons for choosing such a linearization strategy: (1) This builds upon available lift force results for the impermeable channel case, which enables easy generalization to other cross-sections, (2) this takes advantage of the fact that parameter γ is naturally very small for the purposes of linearization (since $|\gamma| \leq 0.01$ in typical microfiltration processes [29]), and (3) such a linearization has prior analytical precedent that suggests an additive decomposition of the lift force into an inertial lift force and a permeate drag force [32].

We write the linearization as

$$\mathbf{F}(\gamma, Re, a/W, x/W, z/W) \sim \mathbf{F}_0(Re, a/W, x/W, z/W)|_{\gamma=0} + \gamma \mathbf{F}_1(Re, a/W, x/W, z/W) + \mathcal{O}(\gamma^2) \quad (4.10)$$

where $\mathbf{F}_0$ is the lift force calculated for a particle at a given location in the absence of any permeate flow (*i.e.*, $\gamma = 0$, which is the standard inertial migration in an impermeable channel) and $\mathbf{F}_1$ represents the first order linearization effect. As indicated earlier, for small γ, we speculate that $\mathbf{F}_1$ is proportional to the drag force, $F_d = 3\pi\mu a U$:

$$\mathbf{F}_1 = \boldsymbol{g}(Re, a/W, x/W, z/W) \times F_d \tag{4.11}$$

where $\boldsymbol{g}(Re, a/W, x/W, z/W)$ encodes the spatial variation across the cross-section. In this work, we do not try to analytically identify the form of the scaling function $\boldsymbol{g}$, but explore how it can be constructed by using a minimal set of full physics simulations. In fact, we show below that $\boldsymbol{g}(Re, a/W, x/W, z/W)$ (and hence, $\mathbf{F}_1$) can be reliably constructed using just two full physics simulations. We rewrite Equation 4.10 (for a fixed Re and a/W) to compute $\mathbf{F}_1$ as:

$$\mathbf{F}_1(Re, a/W, x/W, z/W) = \frac{\mathbf{F}(Re, a/W, \gamma, x/W, z/W) - \mathbf{F}_0(Re, a/W, x/W, z/W)}{\gamma} \tag{4.12}$$

Here $\mathbf{F} - \mathbf{F}_0$ is the difference between the calculated forces maps. $\mathbf{F}$ represents the force vector field of a particle in the presence of a permeate flow at some fixed Re and γ and $\mathbf{F}_0$ is force vector field for the same particle at the same Re but in the absence of permeate flow ($\gamma = 0$). Figure 4.4a shows the spatial distribution of this residual for various values of γ. Interestingly, it appears that these curves are self-similar when scaled by $F_P = 3\pi\mu a\gamma U$, suggesting the utility of the proposed linear model. In figure 4.4b and 4.4c we construct $\boldsymbol{g}$ by dividing the residual $\mathbf{F} - \mathbf{F}_0$ by the characteristic permeate force F_P. In figure 4.4b, keeping Re constant, we see three distinct curves representing our three particle sizes, showing that all normalized residual curves fall on top of each other when divided by γ. Similarly, the curves collapse as shown in figure 4.4c corresponding

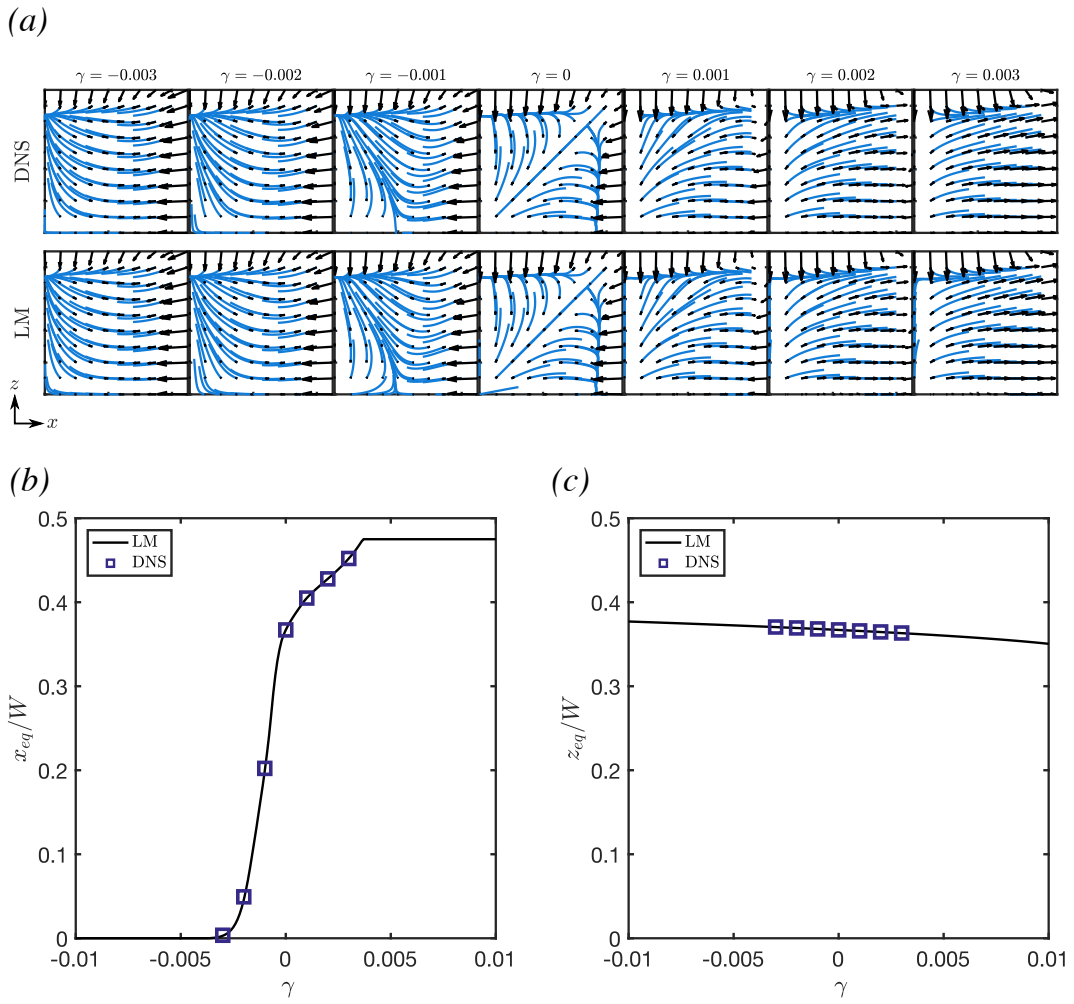

Figure 4.5: (a) Force fields for various values of γ for both the direct numerical simulation (DNS) and the linear model (LM) with a streamline trace overlaid in blue for visualization ($a/W = 0.05$ and $Re = 100$). The bounding box for each field is $0.45W \times 0.45W$ (b) x-equilibrium plotted against the relative permeate flow γ. (c) z-equilibrium plotted against the relative permeate flow γ. The discrete points represent the results from the DNS and the continuous black line is the result of the LM.

to each value of Re (at a fixed a/W). We note that $\boldsymbol{g}$ is insensitive to the choice of Re (figure 4.4c and A.5).

We compare the force maps constructed using $\mathbf{F}_1$ (*i.e.* LM, for linearized model), with that from the full physics simulations (*i.e.* DNS) in figure 4.5a. We chose the interesting case of $Re = 100$ and $a/W = 0.05$, and seven discrete values of γ, where fields yield drastically different 'streamline' morphologies, from a complete wall suction at $\gamma = 0.003$ to center-plane focusing at $\gamma < -0.003$.

First we compute $\mathbf{F}_1$ according to equation 3.3 for each of the six permeate solutions [*i.e.* $\gamma = \pm 0.001, \pm 0.002, \pm 0.003$]. With this result, we average all six $\mathbf{F}_1$ fields to produce a master solution, and thus eliminate any numerical noise that is inherent in this type of model construction. From figure 4.5a, it is apparent that the LM reconstructs the lateral lift force maps qualitatively well with little discernible error; where the advantage of the LM is that it only requires knowledge of a finite number of simulations. More importantly, the LM is not limited to discrete values of γ, but can be used to evaluate forces for continuous values of γ. We next compare the predicted location of the focusing points (force equilibrium points) in figure 4.5b and 4.5c for different γ. In figure 4.5b we see that the x-equilibrium diagram spans a wide range of the channel where the limits are set by the centerline ($x/W = 0$) and by contact with the porous wall ($x/W = 0.475$). Similarly, figure 4.5c shows the z-equilibrium diagram for the same system, where the equilibrium shift is seemingly independent of γ. The LM provides the ability to tune the permeate flow rate, γ to precisely select a desired equilibrium location. This is potentially very useful for particle separation applications.

We next investigate the scaling interplay between the inertial force $\mathbf{F}_0$ and the permeate drag $\gamma\mathbf{F}_1$ with increasing Re and particle size, we note that $\gamma\mathbf{F}_1$ scales as the Stokes drag force *i.e.*, $F_P \sim 3\pi\mu a\gamma U$ and the inertial lift forces scale as $F_L \sim \rho U^2 a^4/W^2$. Hence, when $|F_P| \gg F_L$ we would expect that permeate forces are dominant and the force fields

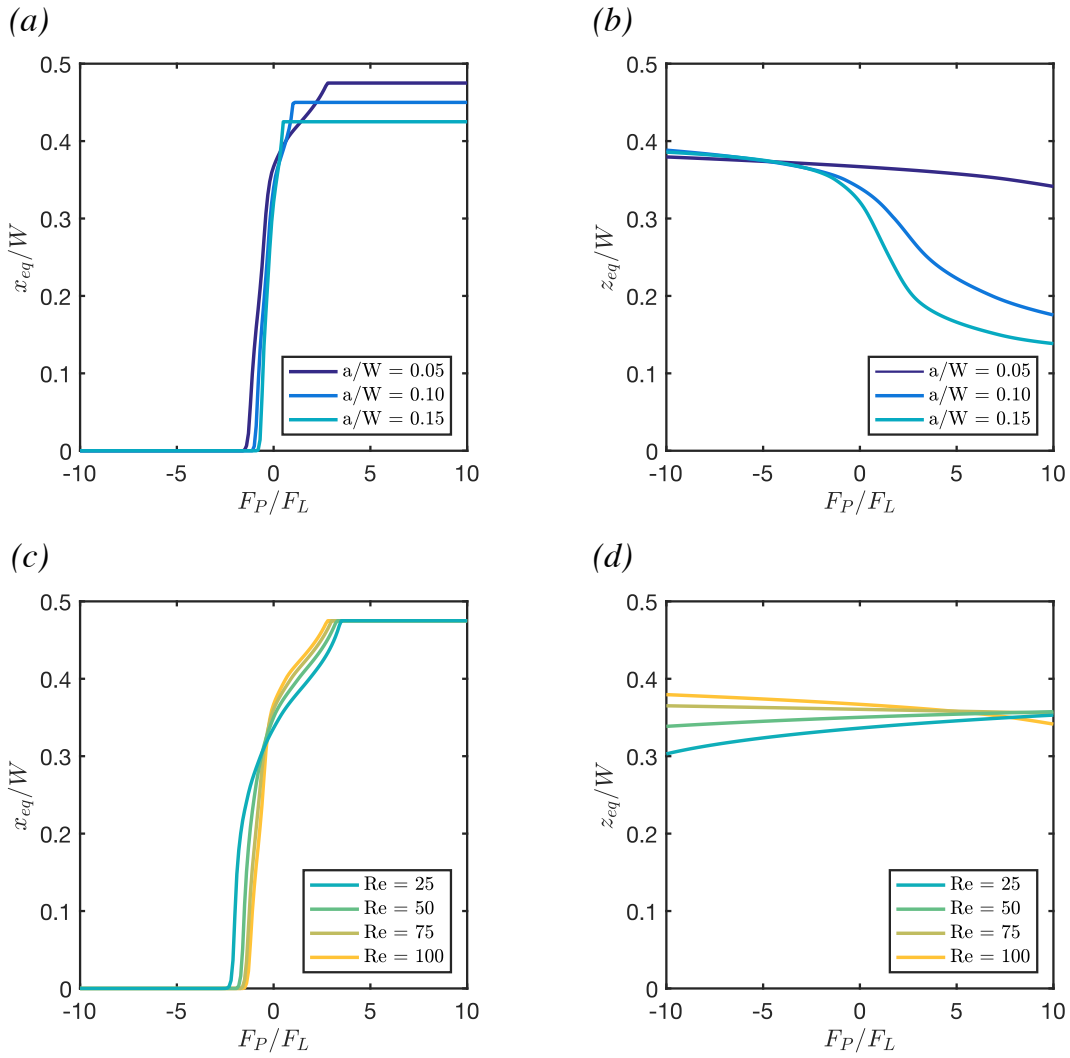

Figure 4.6: (a) x-equilibrium as a function of the relative permeate force (F_P/F_L) for three particle diameters ($a/W = 0.05, 0.10$ and 0.15) at $Re = 100$. Of note is that the data is limited by either the centerline ($x/W = 0$) or the confining walls for large values of ($x/W = 0.50$) (b) z-equilibrium diagram for three particle diameters ($a/W = 0.05, 0.10$ and 0.15). Here the equilibrium shift is less sensitive than the x_{eq} counterpart that is the particle deviate only slightly from the zero permeate equilibrium. (c) x-equilibrium as a function of the relative permeate force (F_P/F_L) for four Re ($Re = 25, 50, 75$ and 100) for a single particle of diameter $a/W = 0.05$. (d) z-equilibrium as a function of the relative permeate force (F_P/F_L) for four Re ($Re = 25, 50, 75$ and 100) for a single particle of diameter $a/W = 0.05$.

would appear as if inertial forces were negligible. Conversely, when $|F_P| \ll F_L$ we would expect that inertial forces would dictate the migration and focusing of a particle in the channel. In figure 4.6 we plot the equilibrium location against the relative permeate force F_P/F_L for all particle size (figure 4.6a and 4.6b) and Re (figure 4.6c and 4.6d). The continuous diagrams seen in figure 4.6 show very clear and specific trends that would be difficult to interpret from discrete DNS data such as that seen in figure 4.3. The equilibrium diagrams shown in figures 4.6a and 4.6c clearly demonstrate the behaviour of a particle at the two extremes as predicted. That is, for large values of magnitude of $|F_P| \gg F_L$ we see a dominance of the permeate flow and the force equilibrium is shifted either to the walls ($x_{eq}/W = (W-a)/2W$) or to the centerline ($x_{eq} = 0$) and on the other extreme, when $|F_P| \ll F_L$, we see that the force equilibrium is only slightly perturbed from the case of no permeate flow. Finally, figures 4.6b and 4.6d show the change in z-equilibrium location as a function of the relative permeate force (F_P/F_L) for a/W and Re. The z_{eq} of large particles are more affected when compared to small particles under this representation of F_P/F_L (figure 4.6b). Further, in figure 4.6d we see that as F_P/F_L increases, the z_{eq} migrates towards the channel wall for low Re and towards the centerline for high Re. This behaviour is indicative of secondary effects that can not be captured by such a simple scaling argument.

4.4.5 Limits of the linear model

We next explore when the additive decomposition of the force into an inertial component and a linear viscous component breaks down. We examine the error in the LM model by comparing the lateral forces of the direct numerical simulation with those constructed with our linear model to determine when nonlinear effects due to γ, Re and a/W cause the model to become unreliable. In figure 4.7a we show a comparison of the inertial force

for three distinct γ at $Re = 100$ and $a/W = 0.10$ and for three distinct Re for $\gamma = 0.2$ and $a/W = 0.10$ (right). As expected, at increasing values of both γ and Re, mismatch between the two models increases. However, the increasing mismatch associated with a change in Re is difficult to discern and so we plot in the inset to figure 4.7b the relative spatial error for each case. We define the error in the LM as:

$$error = \frac{\|\mathbf{F}_{DNS} - \mathbf{F}_{LM}\|_2}{\|\mathbf{F}_{DNS}\|_2} \tag{4.13}$$

Where $\mathbf{F}_{DNS}$ and $\mathbf{F}_{LM}$ are the force distribution calculated using the direct numerical simulation and the linear model respectively. Figure 4.7b shows how the error in the LM increases with a/W, γ and Re. In general, as the permeate Reynolds number Re_{U_W} ($Re_{U_W} = |\gamma|\frac{a}{W}Re$) increases, so does error. This confirms our hypothesis that as both inertial and permeate flow increase, nonlinear effects become more prominent and cannot be captured in our linear model.

Over all sets of data for $Re_{U_W} \leq 1$ the error in the LM is less than 5%, represented by the dashed lines in figure 4.7b. Therefore, in figure 4.7c we determine the maximum $|\gamma|$ for a given $\frac{a}{W}Re$ defined as where error will be 5%. Superimposed on this figure we show the γ (at a given $\frac{a}{W}Re$) at which the particle equilibrium location coincides with the confining walls (*i.e.* wall contact) and therefore an increase in γ will no longer result in a change in particle equilibrium. It is clear that for the particles studied in this work, that we will never reach the 5% error limit of the LM, suggesting that the LM is a viable, useful and applicable model for fast experimental exploration of the effect inertial migration under permeate flow conditions.

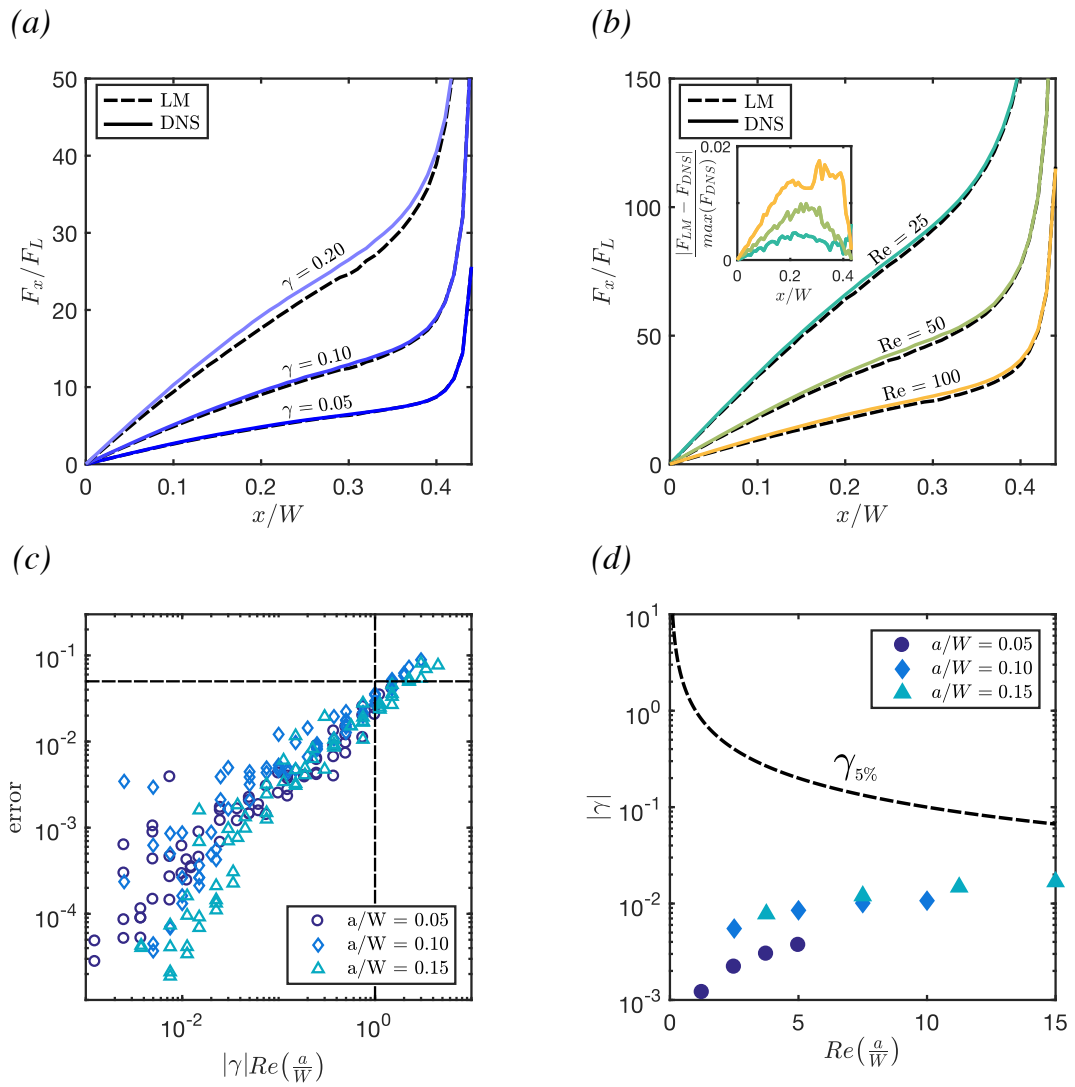

Figure 4.7: A direct comparison of the forces on a particle as computed by a DNS and the LM showing how error in the LM increases with increasing γ (a) and Re (b). It is difficult to see from a direct comparison that the error is increasing with Re therefore, we plot in the inset the local relative error. (c) A plot illustrating how error in the LM increases with the permeate Reynolds number $Re_{U_W} = |\gamma| Re \frac{a}{W}$. The dashed lines shows that for $Re_{U_W} > 1$ error in the linear model is greater than 5%. (d) $\gamma - Re \frac{a}{W}$ operating parameter space for the LM, where using the LM in the space beneath the blacked dashed line should yield less than 5% error in the model. Superposed onto this operating parameter space are data points for the three particle sizes representing the value of $|\gamma|$ at which complete wall suction occurs for the particles studied.

4.5 Experiments

In this section, we illustrate the utility of the linearized model by comparing experiments with predicted trajectories of inertial particles within a porous channel. We microfabricated a model porous system as seen in figure 4.8a. The microfluidic device is composed of a primary channel that is 3.2 cm long with a square cross-sectional area of $100\times100\,\mu$m. The particles enter the channel through a long straight region intended to prefocus the particles. Following this region, there is a permeate region $L = 1.0\,$cm where flow can enter and exit the channel through an array of permeate channels of $W_P = 5\,\mu$m width spaced $\delta = 50\,\mu$m apart, with a length of $L_P = 4.95\,$mm. A two-syringe pump system (Harvard Apparatus) provides both inlet flow and permeate flow: the first pump infuses the inlet flow into the primary channel at a constant volumetric flow rate (Q_F), and the second pump has two possible configurations depending on the ratio $\beta = Q_R/Q_F$. If β is less than one the second pump is placed at the exit of the primary channel and limits the flow rate to a rate of Q_R through the primary outlet. If β is greater than one the second pump infuses flow through the permeate channels at a rate Q_P where $Q_F + Q_P = Q_R$. In general the flow in a device like this is highly dependent on the relative hydrodynamic resistance of the permeate channels to that of the main channel. In our geometry, the permeate resistance is large compared to the main channel and it can be shown that in this limit the volumetric flow rate decreases linearly with axial location, so $Q(y) = Q_F[1 + \frac{y}{L}(\beta - 1)]$ (appendix A.7). Using conservation of mass we find the constant permeate velocity to be $U_W = \frac{Q_F(1-\beta)}{2WL}$, and thus $\gamma(y) = W^2U_W/Q(y)$.

We performed migration experiments with a suspension of $10\,\mu$m fluorescent polystyrene particles in DI water at a concentration of 10^4 particles/ml, and we add 0.5% v/v Tween 20 (Sigma-Aldrich) to reduce particle aggregation. To find the particle locations, we record streak images with a CCD camera (Andor Luca) by accumulating approximately

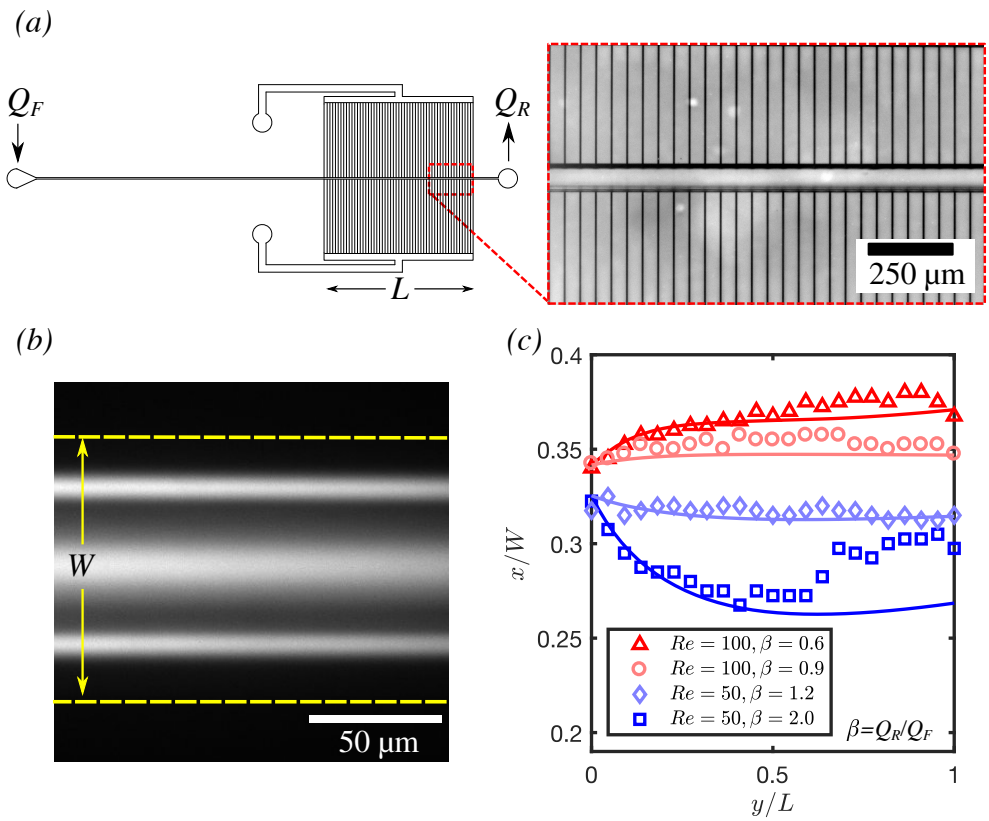

Figure 4.8: (a) schematic showing the microfluidic device composed of a long straight region ($\approx 1.9\,\text{cm}$) followed by a region ($L = 1.0\,\text{cm}$) where there is an array of perpendicular permeate channels (inset) that allow permeate flow to enter or exit the channel. (b) Long exposure image of 10 μm fluorescent polystyrene particles in a 100×100 μm ($W \times W$) channel. The in-plane particles are measured at a distance x relative to the centerline. (c) Comparison of computed (solid lines) and experimentally measured trajectories (shapes) of a particle $a/W = 0.10$ for various operating conditions of the microfluidic device.

25 s of image data at each downstream location and the post-processing using image-processing software (MATLAB). Figure 4.8b shows an example of a streak image. We post process images like this to locate three peaks, the center peak corresponds to the out-of-plane equilibrium while the remaining two correspond to the in-plane equilibrium. Since the in-plane equilibria are symmetric about the centerline, we build a trajectory from one in-plane equlibria at various axial locations along the length of the channel to compare with our LM. More details on the experiments can be found in [2].

Figure 4.8c shows four experimental trajectories of 10 μm particles. The prefocused particles enter the permeate region at $y/L = 0$ and begin to migrate either towards the wall or away, depending on the direction of the permeate flow. Here values of $\beta > 1$ indicate the permeate flow is directed towards the center of the channel and conversely $\beta < 1$ indicates that the flow is directed out of the channel. Even though the permeate flow is constant, the trajectories can be non-monotonic, where the particles begin migrating in one direction and subsequently reverse directions due to the evolving nature of inertial and permeate forces in the spatially varying flow field (figure 4.8c). We can calculate the particle trajectories with our linear model by knowing how the flow parameters (*i.e.* γ and Re) change with axial location in the channel.

We calculated the theoretical trajectories with a first order time stepping approximation (*i.e.* Euler method), evaluating the force at $z = 0$. We do not expect much motion in the z-direction because the lift forces in the z-direction are much smaller than the x-direction lift force for the prefocused stream of particles we are modeling. Thus the equations of motion become:

$$y_{n+1} = y_n + u_y(x_n, z = 0)\frac{Q(y)}{Q_F}\Delta t \tag{4.14}$$

$$x_{n+1} = x_n + \frac{F_x(x_n, y_n, z = 0)}{3\pi\mu a\lambda}\Delta t \tag{4.15}$$

where $u_y(x, z)$ is the flow field in a square channel [61] and $F_x(x, y, z)$ is the predicted force in the lateral direction calculated using our linear model. The axial dependence of the lateral force F_x is calculated by mapping the axial location of the particle to a corresponding local value of Re. With this information, we interpolate between a pre-calculated data set and generate the local zero permeate lift force. Using the observation that g_x is invariant to Re (figure 4.4c and A.5), we construct the linear model using

equation 4.10. Finally, λ is the correction factor for Stokes' drag near a confining wall (appendix A.6). Using the linear model we are able to reproduce the experimental trajectories reasonably well (figure 4.8c), further proving the viability of our linear model.

4.6 Conclusion

Our findings describe the spatially inhomogeneous forces on confined inertial particles in the presence of a permeate flow. Our numerical simulations suggest that the relative permeate force (F_P/F_L) is an important parameter in the characterization of behaviour of these particles. For very small magnitudes of the relative permeate force the location of force equilibrium remains unchanged and reminiscent of flow in a nonporous duct. As the magnitude of the relative permeate force is increased, the equilibrium position deviates further from the non-porous case until it is either limited by the wall or centerline. Using the results from our numerical simulations we are able to construct a model which superposes the linear viscous effects of the permeate flow to that of the underlying inertial forces. This linear model shows excellent agreement over a continuous span of permeate flow with both full simulations and experimental observations when $Re_{U_W} < 1$ with no added computational penalty. This is especially noteworthy because the flow field in a channel with permeable walls is not trivial and would normally require much effort to simulate with another approach. We speculate that this model can help rapidly design microfluidic devices that can precisely manipulate particle streams. Furthermore, the framework for our linear model presented in this work can also be implemented in other systems where external forcing of inertial particles exists such as with magnetic or electric forces. Our model greatly reduces the complexity of a well studied and ubiquitous flow. We emphasize the fact that the linearization, while useful, does not account for potentially important phenomena like particle deformability and non-Newtonian suspending fluids,

which are typical of real world systems. Developing similar simple and computationally efficient methods for accounting for such interactions is a future area of research work.

Chapter 5

A model for interial focusing of particles in curvilinear microchannels

5.1 Abstract

The behavior of confined particles in curvilinear microchannels at moderate Reynolds number has received much attention in recent years. This interest has been motivated by applications such as the separation and concentration of bioparticles. However, the ability to design a curvilinear channel for a specific application is often based on empirical results, as no complete theoretical model currently exists. In this chapter we numerically model the flow physics of a particle in a curvilinear channel. To do so we borrow from the model presented in Chapter 4, that is we choose a reference frame that is rotating with the particle and include both Coriolis and centripetal forces. Here we investigate the three dimensional focusing behavior of inertial particles and the applicability of the point particle assumption previous researchers have proposed. Finally, we propose a new model that takes into account the full physics, but relies on a perturbation expansion of the lateral forces, where the perturbation parameter is the curvature ratio of the channel. The insight gained through this fundamental study can be applied in the design of new separation devices for a wide plethora of applications by non-experts in the field of fluid

mechanics.

5.2 Introduction

It has long been known that particles flowing at a finite Reynolds number (Re) have the tendency to passively migrate laterally across streamlines and focus at stable equilibrium locations [18]. The phenomena is a result of the nonlinear fluid stresses that act on a confined particle to produce a lateral motion and focusing [19]. Recently, this phenomena has received a new found interest due to its use in the precise manipulation of micron-sized particles in a continuous microflow. Researchers have designed many unique devices to isolate [62], sort [23], focus [63, 64] and concentrate [26] particles on the basis of inertial microfludics. By far the most common device designs leverage curvilinear channels to produce a transverse Dean flow, allowing for exquisite control of particle streams by simply tuning the Dean forces. The Dean flow is a consequence of the curvilinear geometry which introduces a centrifugal acceleration component directed radially outward as flow navigates through the curved channel. The resulting Dean flow is orthogonal to the streamwise flow direction and is composed of two symmetric-counter rotating vortices known as Dean vortices (figure 5.1a). The effect of these vortices in combination with inertial forces serve to perturb the inertial equilibrium locations of a particle into a size dependent stream. The magnitude of this perturbation is set by the strength of these vortices, which is dictated by the Dean number (De) [65, 66, 67].

Inertial Dean flow focusing has been used with both alternating curves and spirals for various bio-analytic purpose [14, 64, 3, 68, 69, 70]. However, modeling the flow in these devices for a specific application is quite challenging as the full Navier-Stokes equations are needed to solve for the particle dynamics in these complex channels. Often complete models are too computationally burdensome to be of any practical use in de-

signing these devices [71]. Given the complexity of simulating particle migration, some authors have proposed the use of lattice Boltzmann methods (LBM) as the technique very computationally efficient [53, 72]. However, LBM is prone to instability issues because of the coarse grained representation of the fluid-boundary interface [72]. By far the most common approach has been a point particle model, where the inertial component is solved for in a straight channel and is added to a Dean flow component. The Dean flow component of the force is solved separately by assuming that is is simply a Stokes drag associated with the underlying Dean flow [3, 68, 73, 74, 75]. The technique is quick and has shown some success, but the ability to superpose these two forces may not hold under certain flow regimes. In particular, it becomes questionable at high De where the Reynolds number based upon the Dean flow velocity (Re_D) approaches unity (figure 5.1b) and inertial corrections to Stokes drag are necessary. Furthermore, at higher De, their is also a redistribution of the axial flow profile (figure 5.1c) that can alter the shear gradient lift forces. Recently, Dinler and coworkers [76] have proposed the use of a direct numerical simulation (DNS) model, where the flow problem is solved in reference frame fixed to a moving sphere simliar to [1, 76, 75, 57]. This method is robust and provides the inertial force distribution over the particle in a section of the channel. This method is well suited for fundamental studies [1], but not for practical design because the it is computationally inefficient. It is no surprise then that Diner *et al.* applied this model in a curvilinear geometry using coarse parameters and an incomplete description of the momentum equations [76].

There is a need for a simple and precise model that can reliably predict the behavior of confined inertial particles across a wide range of flow parameters in a curvilinear geometry. To address this need we first use a numerical model similar to [76], but include Coriolis and centripetal terms in our momentum equations. Based on our numerical observations, we then develop a perturbation based model to predict the lateral forces acting on a

neutrally buoyant spherical particle migrating in curved channel. We then validate this model against previously published experiments, and compare to the Stokes drag model proposed in the past. Finally, we use this model to design a spiral channel and speculate on how this model can be used to design devices in the future.

5.3 Numerical Model

In order to understand the inertial focusing and the effects of the Dean flow in curved microchannels it is necessary to study an idealized system where the individual components of the forces can be determined. The model in this chapter focuses on the flow of a neutrally buoyant particle of diameter a in a channel of rectangular cross-section $W \times H$ ($W/H = 2$), arc-length $5W$ and average radius R (figure 5.1a). The particle is translating with at a velocity $\mathbf{U}_P = -U_p\mathbf{e}_\theta = U_p[-\cos\theta\mathbf{e}_x, 0\mathbf{e}_y, \sin\theta\mathbf{e}_z]$ and angular velocity $\mathbf{\Omega}$ in a flow of average velocity U. We define the channel Reynolds number as $Re = \rho U D_h/\mu$ the relative curvature of the channel as $\delta = D_h/2R$, and the Dean number as $De = Re\sqrt{\delta}$, where ρ and μ are the fluid density and viscosity respectively and $D_h = 2(W+H)/(WH)$ is the hydraulic diameter of the channel.

To solve for the flow field and pressure around the particle, it is convenient to consider a rotating frame of reference such that the particle appears stationary. The rotating reference frame is a non-inertial frame of reference and thus the Navier-Stokes equations adopt a form that takes into account the effects of centripetal and Coriolis forces. Note that we assume a quasi-steady model and thus the time dependent terms vanish from the Navier-Stokes equations (appendix A.8):

$$\rho\mathbf{u}\cdot\nabla\mathbf{u} = \mu\nabla^2\mathbf{u} - \nabla p - \rho\big(2\dot{\boldsymbol{\theta}}\times\mathbf{u} + \dot{\boldsymbol{\theta}}\times\dot{\boldsymbol{\theta}}\times\mathbf{r}\big) \tag{5.1}$$

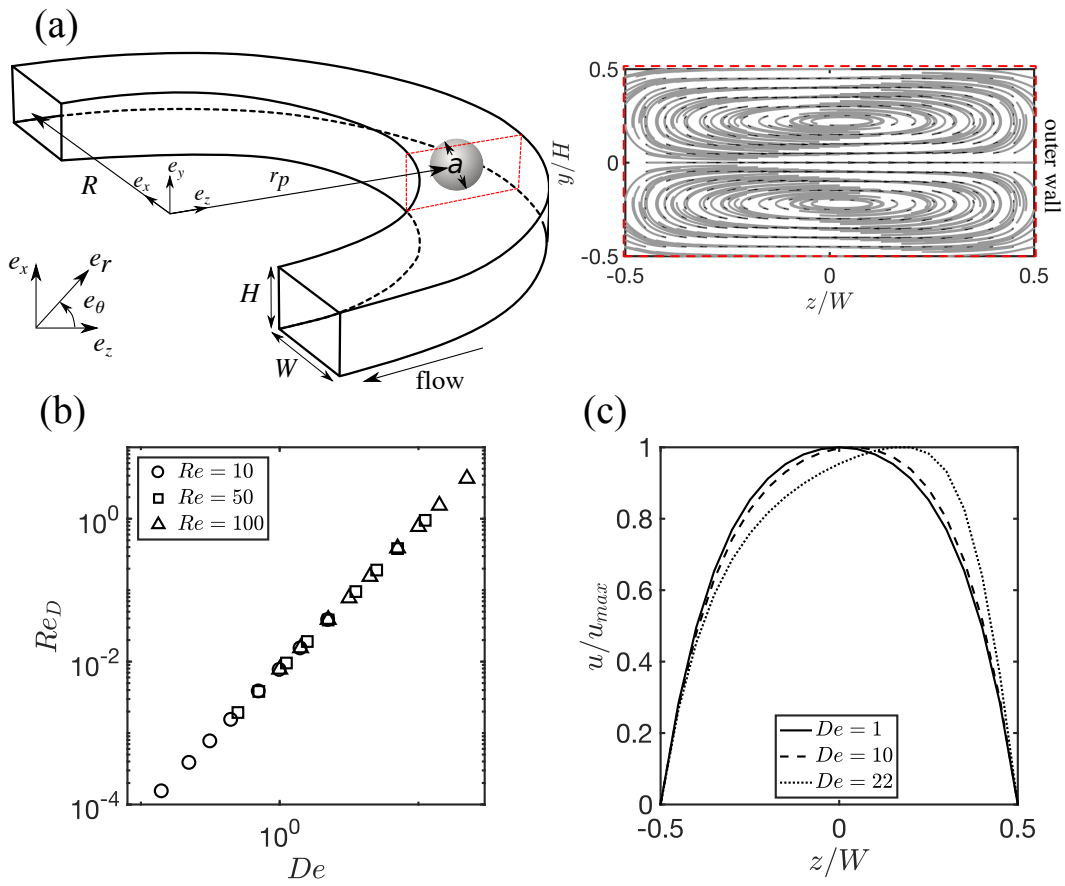

Figure 5.1: (a) Schematic illustration of the channel considered in this chapter. The channel is rectangular with cross-section ($W \times H$) and average radius R. The spherical particle of diameter a flows within the confines of the bounding walls at a location $\mathbf{r}_p$ relative to origin. A cross sectional slice of the channel reveals that the recirculating flow patterns shown in the red dashed window. (b) A plot of the Reynolds number (Re_D) of this recirculating flow versus the Dean number (De). For high De the flow has appreciable inertia as the Re_D is $\mathcal{O}(1)$.(c) A plot of the axial flow profile for various De. For low De we observe a symmetric profile similar to flow in a straight channel, but for high De the symmetry vanishes due to increased flow redistribution associated with the Dean flow.

$$\nabla \cdot \mathbf{u} = 0 \tag{5.2}$$

where p is the fluid pressure field, $\mathbf{u}$ is the fluid velocity field in the rotating reference frame, $\dot{\boldsymbol{\theta}}$ is the angular velocity of the frame, and $\mathbf{r}$ is the position vector of a fluid element about the point of rotation of the frame. The frame velocity, $\dot{\boldsymbol{\theta}}$ is related to the particle

velocity by: $\mathbf{U}_p = \mathbf{r}_p \times \dot{\boldsymbol{\theta}}$, where $\mathbf{r}_p$ is the position vector of the particle center relative to the point of rotation (*i.e.* at the origin).

In a manner similar to Chapter 4, the rates of the suspended particle (U_P and $\boldsymbol{\Omega}$) can be self-consistently determined by setting conditions such that the axial motion satisfies a drag constraint $F_\theta = 0$ (equation 4.3) and its rotational motion satisfies a torque constraint $\tau_r = \tau_z = \tau_\theta = 0$ (equations 4.4). The boundary conditions of this problem are in the rotating reference frame. Therefore, the no slip condition on the walls is:

$$\mathbf{u} = -\dot{\boldsymbol{\theta}} \times \mathbf{r} \quad \text{on all walls} \tag{5.3}$$

The no slip condition on the particle is enforced by assigning a velocity to the surface of the sphere corresponding to that of a rigid body rotation at angular velocity $\boldsymbol{\Omega}$

$$\mathbf{u}_{surface} = \boldsymbol{\Omega} \times (\mathbf{r} - \mathbf{r}_p) \tag{5.4}$$

Finally, far from the particle the flow is undisturbed and regains the behavior of flow in the absence of a particle. To solve for the unknowns (*i.e.*, $\mathbf{u}$, p, U_p and $\boldsymbol{\Omega}$) we couple the Navier-Stokes equations to the equations constraining the particle motion (*i.e.* torque and force free equations of motion) and solve directly using the COMSOL multiphysics software. This procedure is performed for a lattice of discrete positions of the particle within the cross-section of the channel (using only the top half of the crossection via symmetry arguments to minimize computational effort). To calculate the lift force on the particle, we integrate the surface stresses on the particle in the appropriate direction (y or z) according to equation 4.9 [1].

[1]Note that because the particle is placed at $\theta = 0$ the forces in the radial direction become force in the z-direction upon transformation of the coordinate system.

5.3.1 Equations of motion

The numerical model outlined in the section above can be used to calculate the hydrodynamic inertial lift forces on a small rigid sphere. This model restrict the motion of a particle in the lateral direction that and calculates the forces that would lead to migration. However, it neglects the contribution of other forces (*e.g.* lateral drag, centripetal and Coriolis forces). To reconcile this difference we start by considering the equations of motion and noting that the velocity of a body is not measured to be the same in the inertial and rotating frame.

$$\mathbf{U}_{p,i} = \mathbf{U}_{p,r} + \dot{\boldsymbol{\theta}} \times \mathbf{r}_p \tag{5.5}$$

Here $\mathbf{U}_{p,i}$ and $\mathbf{U}_{p,r}$ are the inertial and relative velocity of the particle, respectively, which in general may also include the migration velocity. Where the equations of motion for a particle are:

$$m_p \frac{d}{dt}\big(\mathbf{U}_{p,i}\big)_i = \int_s \mathbf{n} \cdot \hat{\mathbf{T}}\, ds \tag{5.6}$$

The left hand side of equation 5.6 are the inertial forces, where m_p is the mass of the particle, and right hand side represents the hydrodynamic forces. $\hat{\mathbf{T}}$ is the total stress tensor of the flow around a particle that is not restricted from moving laterally. Note that we neglect any gravity force because the particle is neutrally buoyant. Then substituting equation 5.5 into equation 5.6 we obtain:

$$m_p \frac{d}{dt}\big(\mathbf{U}_{p,i}\big)_r + \dot{\boldsymbol{\theta}} \times \mathbf{U}_{p,i} = \int_s \mathbf{n} \cdot \hat{\mathbf{T}}\, ds \tag{5.7}$$

Applying equation 5.5 to this result yields:

$$m_p\left[\frac{d}{dt}\left(\mathbf{U}_{p,r}+\dot{\boldsymbol{\theta}}\times\mathbf{r}_p\right)_r+\dot{\boldsymbol{\theta}}\times\left(\mathbf{U}_{p,r}+\dot{\boldsymbol{\theta}}\times\mathbf{r}_p\right)\right]=\int_s\mathbf{n}\cdot\hat{\mathbf{T}}\,ds \tag{5.8}$$

Assuming that the rate of rotation is constant the equations of motion become:

$$m_p\frac{d}{dt}\left(\mathbf{U}_{p,r}\right)_r=\int_s\mathbf{n}\cdot\hat{\mathbf{T}}\,ds-m_p\left[2\dot{\boldsymbol{\theta}}\times\mathbf{U}_{p,r}+\dot{\boldsymbol{\theta}}\times(\dot{\boldsymbol{\theta}}\times\mathbf{r}_p)\right] \tag{5.9}$$

We can simplify this result by considering that the axial component of the particle's velocity is much greater than the lateral migration velocities and thus the Coriolis forces are negligible in comparison to the centripetal forces.

$$\dot{\boldsymbol{\theta}}\times\mathbf{U}_{p,r}\ll\dot{\boldsymbol{\theta}}\times(\dot{\boldsymbol{\theta}}\times\mathbf{r}_p). \tag{5.10}$$

Furthermore, if we assume that the particle is not accelerating in the rotating reference frame (quasi-steady) than the equations of motion reduce to:

$$0=\int_s\mathbf{n}\cdot\hat{\mathbf{T}}\,ds-m_p\dot{\boldsymbol{\theta}}\times(\dot{\boldsymbol{\theta}}\times\mathbf{r}_p) \tag{5.11}$$

The hydrodynamic contribution in equation 5.11 has been the subject of many fundamental studies [77]. The most notable of which was a rigorous derivation by Maxey and Riley [78]. They formulated an expression for the hydrodynamic contribution that was decomposed into several independent components: Stokes drag, buoyancy, a pressure gradient (accounting for effects of the undisturbed flow), the virtual mass (accounting for the acceleration of the displaced fluid), and a history term (accounting for the initial conditions of the particle). However, this transient equation of motion for particles did not capture the lateral migration forces because they were derived in the low Re limit and neglect and effect of particle rotation.

In this work we assume that: i) Our numerical model includes the pressure gradient term, as the pressure field is inherent to the solution of the flow problem. ii) We can neglect the buoyancy term because the particle density is identical to the fluid density. iii) We can neglect the virtual mass and history terms because the Stokes number is small ($St \ll 1$). iv) The hydrodynamic stress on the surface of the particle can be decomposed into the hydrodynamic lift and drag, that is to say:

$$\int_s \mathbf{n} \cdot \hat{\mathbf{T}}\, ds = \int_s \mathbf{n} \cdot \mathbf{T}\, ds - \mathbf{F}_{drag} \tag{5.12}$$

The first term on the right hand side represents the forces calculated using our quasi-steady numerical model, while the second term is the force required to move a sphere in quiescent channel at the velocity $\mathbf{U}_{p,r}$. Using these assumptions, the final form of the equations of motion are:

$$0 = \mathbf{F}_{DNS} - \mathbf{F}_{drag} = \int_s \mathbf{n} \cdot \mathbf{T}\, ds - m_p \dot{\boldsymbol{\theta}} \times (\dot{\boldsymbol{\theta}} \times \mathbf{r}_p) - \mathbf{F}_{drag} \tag{5.13}$$

In the following sections we consider the spatial representation of $\mathbf{F}_{DNS}$ in the lateral directions for various combinations of the flow parameters Re and δ.

5.3.2 Numerical results

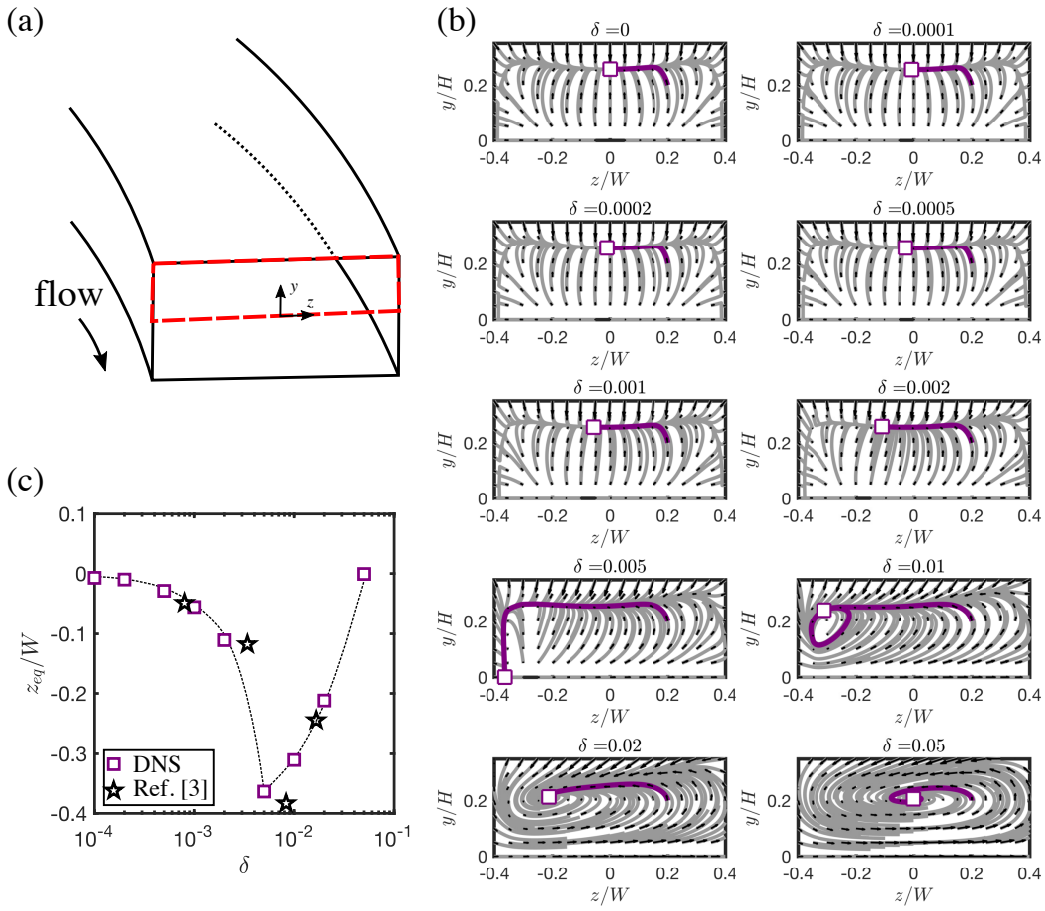

Figure 5.2: (a) Schematic illustration of a curved channel depicting the region of interest (red dashed box).(b) The cross-section plots show the simulated resultant force $\mathbf{F}_{DNS}$ on the particle for multiple channel geometries ($\delta = D_H/2R$) at $Re = 100$. The grey line are streamlines of the force field and are for visualization purposes. The purple lines are arbitrary streamlines (seeded at $z/W = y/H = 0.2$) that show the trajectory a particle would take as it moves towards a stable equilibrium (squares). (c) Stable equilibrium location as a function of the relative channel curvature δ for the results of this numerical model and experiments done by Martel *et al.*, 2013 [3].

The numerical model presented in this chapter investigates the steady state forces $\mathbf{F}_{DNS}$ on a finite sized particle through direct numerical simulation of the flow field with a particle. This model includes finite size effects, the redistribution of the axial velocity profile and the Coriolis/centripetal acceleration terms in the momentum equa-

tion. Figure 5.2a shows a schematic illustration of the top half of the channel cross-section over which we simulate a particle spanning the parameters $Re = [10, 50, 100]$ and $\delta = [0, 0.0001, 0.0002, 0.0005, 0.001, 0.002, 0.005, 0.01, 0.02, 0.05]$. Figure 5.2b plots the force-field $\mathbf{F}_{DNS}$ for a subset of the simulation space, that is for an intermediate sized particle ($a/D_h = 0.15$) and at $Re = 100$. Under these conditions, and without loss of generality, we observe that the force-fields are progressively perturbed for increasing channel curvature (*i.e.* δ) at a constant flow rate ($Re = 100$) (figure 5.2b). Further, in a straight channel (*i.e.* $\delta = 0$) we see four stable equilibrium locations, where the equilibrium along the long faces (LFE) attracts more streamlines than the equilibrium along the short faces (SFE). The phenomena of a relatively more stable LFE has been observed experimentally and numerically for a rectangular channel under the similar conditions [54]. As the channel curvature increases, the location of the LFE shifts towards the inner wall until. The LFE eventually merges with the SFE at sufficiently high channel curvature ($\delta = 0.005$). After this point the SFE/LFE begins a retrograde motion towards the outer wall (figure 5.2c). Interestingly, after the SFE/LFE switch direction, the equilibrium destabilizes. At this point the particle is not focused at a single point, but rather orbits in plane (figure 5.2b, $\delta = 0.01$). These results are compared to the experiments of Martel *et al.* [3] and show excellent agreement.

The non-monotonic shift in LFE at a fixed Re for varying δ is caused by the presence of the Dean flow within the channel [75]. Initially, for low δ the LFE is at a vertical location where the Dean flow is directed towards the inner wall. The strength of this Dean flow increases with the curvature of the channel (figure 5.1b) and thus the LFE shifts towards the inner wall with increasing δ. As LFE the shifts towards the inner wall the Dean flow in that region beings to impart a vertical force that is directed in the negative y-direction (figure 5.1a). This causes the LFE to move towards the SFE and eventually merge. Finally, the merged LFE/SFE migrate towards the outer wall (locally

the direction of the Dean flow) at sufficiently high De. This transition occurs because the shear gradient across the width of the channel on the inner half of the channel is insufficient to counter the increasing Dean flow forces; thereby adjusting the location of the LFE/SFE towards the center-line [3].

5.3.3 Second order perturbation model

The process of solving for the inertial forces with the numerical model proposed in the previous subsection is computationally challenging. Therefore, we propose a model that can produce quantitatively results, but with significantly less computational requirements. This model is based on the observation that the inertial forces are increasingly perturbed for increasing channel curvature (figure 5.2). Dean's seminal study laid the framework for analytic solutions for flow in curved channels [67]. He used the perturbation method, with the curvature ratio as the perturbation parameter to describe the flow in a curved pipe. Following the work of Dean, we propose a similar model, which assumes that the forces on a particle (and not the flow) in a curved geometry can be thought of as a perturbation series. Like Dean's model the leading term in this power series is the solution of the straight channel problem, while further terms describe the deviation in the solution due to increased curvature δ.

We first consider a perturbation of the lateral lift forces $\mathbf{F}_{DNS}(\delta, Re, a/D_h, y/H, z/W)$ about the $\delta = 0$, *i.e.* straight channel case.

$$\mathbf{F}_{DNS} \approx \mathbf{F}_0 + \delta\mathbf{F}_1 + \delta^2\mathbf{F}_2 + \mathcal{O}(\delta^3) \tag{5.14}$$

Where $\mathbf{F}_0 = \mathbf{F}_{DNS}\big|_{\delta=0}$ is the full physics lift force calculated for a particle under a given Re for a straight channel (*i.e.*, $\delta = 0$), $\mathbf{F}_1$ and $\mathbf{F}_2$ represents the effects of channel curvature on the lateral forces experienced by a particle. We speculate that for sufficiently

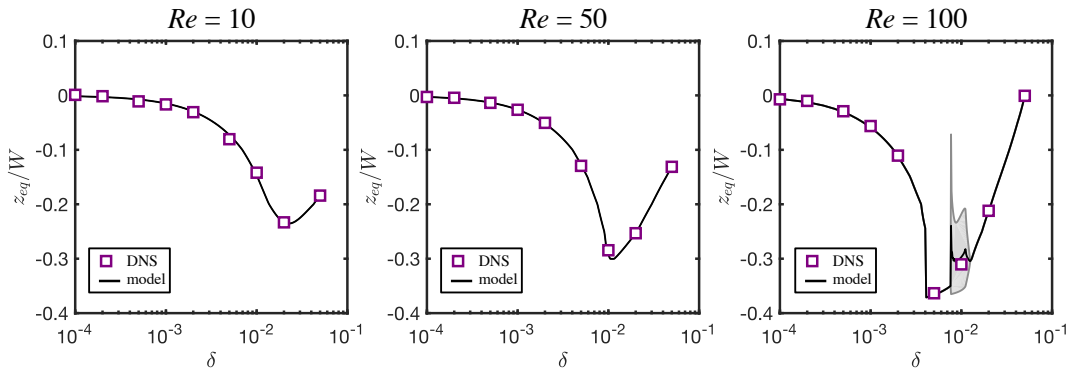

Figure 5.3: Stable equilibrium location as a function of the relative channel curvature δ for three distinct Re and $a/D_h = 0.15$. The square markers represent results from direct numerical simulations (DNS) and the solid lines represent the results from the second order perturbation model (model). The shaded region at $Re = 100$ represents the orbit focusing limits.

small δ, $\mathbf{F}_1$ and $\mathbf{F}_2$ in equation 5.14 are the only terms required to model the lateral forces and thus we neglect any higher order terms. In this work, we do not try to analytically identify the form of the functions $\mathbf{F}_1$ and $\mathbf{F}_2$, but explore how it can be constructed by using a minimal set of full physics simulations. We show below that $\mathbf{F}_1$ and $\mathbf{F}_2$ (and hence, $\mathbf{F}$) can be reliably constructed using just three full physics simulations - to do so we solve for these perturbation functions by rewriting equation 5.14 for a fixed Re and a/D_h.

$$\mathbf{F}_1 = \frac{\left(\delta_1^2\mathbf{F}_0 - \delta_2^2\mathbf{F}_0 - \delta_1^2\mathbf{F}_{DNS}\big|_{\delta=\delta_2} + \delta_2^2\mathbf{F}_{DNS}\big|_{\delta=\delta_1}\right)}{\delta_1(\delta_2^2 - \delta_1\delta_2)}$$

(5.15)

$$\mathbf{F}_2 = -\frac{\left(\delta_1\mathbf{F}_0 - \delta_2\mathbf{F}_0 - \delta_1\mathbf{F}_{DNS}\big|_{\delta=\delta_2} + \delta_2\mathbf{F}_{DNS}\big|_{\delta=\delta_1}\right)}{\delta_1(\delta_2^2 - \delta_1\delta_2)} \tag{5.16}$$

Here $\mathbf{F}_{DNS}\big|_{\delta=\delta_1}$ and $\mathbf{F}_{DNS}\big|_{\delta=\delta_2}$ are the full physics simulation results for flow at the same Re in two distinct channels of curvature ratio $\delta = \delta_1$ and $\delta = \delta_2$ respectively.

To demonstrate the utility of such a model, we calculate $\mathbf{F}_1$ and $\mathbf{F}_2$ using equations 5.15 and 5.16 with only three DNS ($\delta = 0, 0.02, 0.05$) at a fixed Re and a/D_h. Figure 5.3 shows the results of this model. Where we show the predicted equilibrium location and compare to DNS results for the three distinct flows (Re). From this figure, it is apparent that the second order model reconstructs the lateral lift force maps well with little discernible error; where the advantage of the model is that it only requires knowledge of three full simulations. Moreover, the model is not limited to discrete values of δ - as it can predict the particle behavior at any combination of δ or Re provided that basis are known. The second order model is so precise that it even predicts the orbit focusing for $Re = 100, \delta = 0.01$ that was observed previously in figure 5.2b; It does so with no knowledge of the flow as $\delta = 0.02$ and $\delta = 0.05$ were used to solve for the model parameters (figure 5.3, $Re = 100$).

5.4 Model Comparison

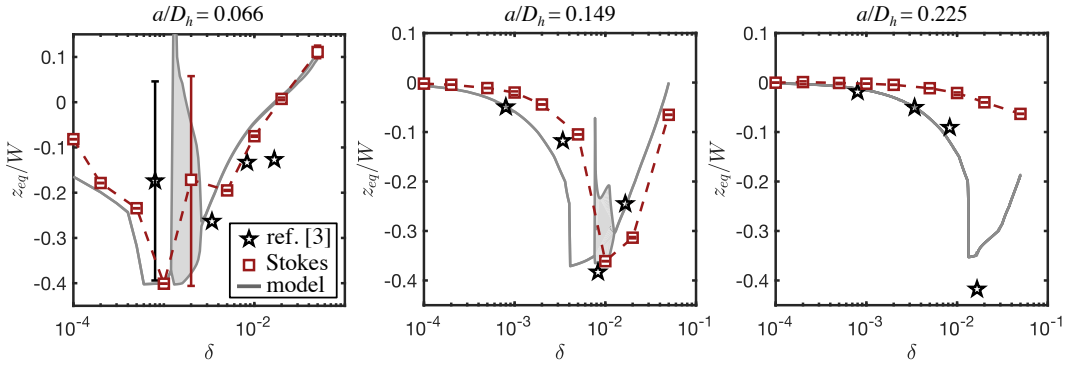

Figure 5.4: Stable equilibrium location as a function of the relative channel curvature δ for three distinct particle size (a/D_h) at $Re = 100$. The square markers indicate the predictions from a simple Stokes drag model (Stokes). The solid lines are the predictions from the second order model (model). The stars represent the experimental results from Martel *et al.* [3].

In this section we compare the results of our model with a simple Stokes model

and experimental results of Martel *et al.* [3]. The Stokes model has been proposed in previous studies as a quick an reliable method for modeling the lateral forces on a particle in curvilinear channel. The Stokes model adds the inertial lift forces ($\mathbf{F}_0$), derived for a straight channel, with a force caused by the Dean flow velocity ($\mathbf{U}_{Dean}$) in the channel. Here $\mathbf{U}_{Dean}$ is the flow field in a channel with no particle at discrete values of δ and Re.

$$\mathbf{F} = \mathbf{F}_0 + 3\pi\mu a\mathbf{U}_{Dean} \tag{5.17}$$

Of note is that the centripetal force has been neglected in this model and in previous work [3, 68, 73, 74, 75]. It is a serendipitous occurrence and can be shown that for a small and neutrally buoyant particle that the pressure gradient term associated with the undisturbed flow imparts a force that exactly cancels out centripetal forces [79, 80]. While this model has been proposed as a simple tool and used heavily in literature, the validity of it has yet to be tested. Particularly, for large particles and at high Re where some of the assumption in this model are no longer valid.

Figure 5.4 shows a comparison of the predicted focusing location for the two models discussed in this chapter with the experimental results of Martel *et al.* [3]. The second order model agrees well with all experimental results. Where in general a small addition of curvature causes the particles to migrate towards the inner wall. However, for the smallest particles ($a/D_h = 0.066$ and $a/D_h = 0.149$), at a sufficiently high curvature, we observe that the particles are entrained in an orbit and not a single focusing location. As expected, for small particles the Stokes model and second order model agree well, but for larger particles and at higher δ, the predicted focusing locations begin to diverge. This discrepancy is attributed to two factors: 1) the redistribution of the axial flow profile at high Dean number, $De = Re\sqrt{\delta}$ and 2) finite size effects which are not considered by the point particle assumption inherent in the Stokes model. Our findings resolve confusion

about the size dependence of inertial lift forces combined with Dean flow experienced by particles traveling through curved microchannels. Many studies have assumed that this behavior can be represented by a simple Stokes model. However, by numerically dissecting the equations of fluid flow around the particle, we find that this assumption does not hold for larger particles.

5.5 Modeling of a spiral channel

To demonstrate one potential application of the model proposed in this chapter, we consider the focusing of particles in a "spiral channel". The spiral channel is a geometry that is ubiquitous in inertial microfluidics. The geometry has been utilized in numerous studies to manipulate particles [65, 69, 70, 3, 81]. However, modeling the focusing behavior of particles in type of channel is typically quite challenging. The challenge is due to the fact that the channel does not have a single radius, but rather a radius that is evolving with the streamwise direction. Modeling the flow in this type of channel using the techniques outlined in the introduction of this chapter would be in feasible as the 3D geometry has a very large aspect ratio. The computational time and memory requirements would be extensive. However, the second order model is well suited for this problem. The second order model predicts local force values and is parameterized by only the local curvature. Thus providing precise force predictions with no knowledge of the flow field everywhere in channel.

Here we consider an Archimedean spiral (figure 5.5a) with a simlar cross-section as the previous section (*i.e.* $W \times H$) that is parameterized by:

$$R = a + b\theta \tag{5.18}$$

Where R is the local channel radius, a is the channel radius at the inlet ($\theta = 0$) and b is a parameter that controls the spacing between spirals. To determine the lateral forces on a particle, we first use equation 5.18 to to derive and expression for relative channel curvature everywhere in the channel:

$$\delta = \frac{D_h}{2(a + b\theta)} \tag{5.19}$$

From equation 5.19 it apparent that curvature can vary significantly over the length of then channel. In figure 5.5b we show this variation in a polar coordinate representation from the inlet to the outlet of this spiral channel. We can then compute the lateral forces using equation 5.17 and coupling it with the result from equation 5.19.

Next, we calculate the trajectories of particle in this geometry with a first order time stepping approximation.

$$\theta_{n+1} = \theta_n + \frac{u_\theta(y_n, z_n)}{R}\Delta t \tag{5.20}$$

$$y_{n+1} = y_n + \frac{F_y(y_n, z_n)}{3\pi\mu a}\Delta t \tag{5.21}$$

$$z_{n+1} = z_n + \frac{F_z(y_n, z_n)}{3\pi\mu a}\Delta t \tag{5.22}$$

Where u_θ is the streamwise flow field, F_y and F_z are the predicted forces in the lateral directions calculated using the second order model. Figure 5.5c and 5.5d show the the trajectories calculated for three distinct particles $a/D_h = 0.066, 0.149, 0.225$ at the same flow rate ($Re = 100$). As a basis for comparison we choose an arbitrary common location to seed the particles ($z/W = 0, y/H = 0.1$). Interestingly, we see that the particles never reach an equilibrium, but rather are constantly migrating (figure 5.5d). This result is

rationalized by considering that the curvature is never constant and thus the forces on the particles are ever evolving. These results agree well with experimental findings, where the focused particle streaks in a simlar spiral channel were seen to continuously migrate [81]. Furthermore, we note that the trajectory is high oscillatory for small particles, but the oscillations dampen towards the outlet. Suggesting that smaller particles in this particular geometry may not focus properly. Finally, an intriguing observation of this channel is observed separation of the focused particle trajectories. For particles seeded in the exact location we observe a significant discrepancy in outlet focusing location between all three particles – suggesting that this may be a viable channel for separation purposes.

This section was purely an exercise in the utility of the proposed model. It is clear that there is tremendous value in predicting the lateral forces in an arbitrary geometries such as the spiral channel presented here. One could imagine easily iterating over thousands of channels to obtain the optimal design for separating particle "A" from particle "B" in minutes. Such a tool can be used to simplify the complex focusing dynamics observed in many previous studies. This chapter provides a deeper quantitative analysis of inertial focusing in spiral channels as well as establishing the framework for channel optimization model.

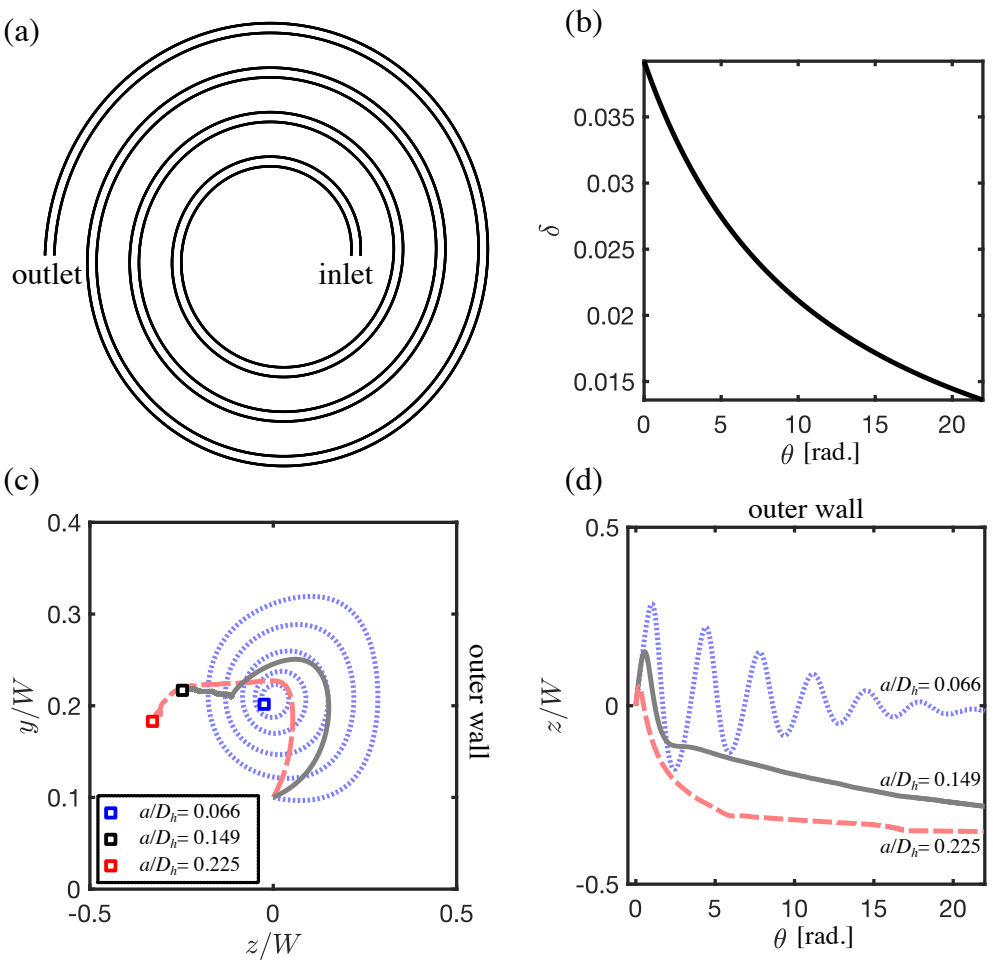

Figure 5.5: (a) Schematic illustration of the spiral channel considered in this chapter. (b) The radius of curvature in this spiral channel decreases in the stream-wise direction as $\delta \sim 1/\theta$. at the inlet $\delta = 0.392$ and at the outlet $\delta = 0.136$. (c) The cross-sectional trajectories of the three particles in this spiral channel at $Re = 100$. The particles are seeded at a common reference and their outlet location is indicated by the square markers. (d) A projection of the particle trajectories in (c) onto the stream-wise plane from inlet ($\theta = 0$ to outlet $\theta = 7\pi$).

5.6 Conclusion

There is a clear need for a simple yet precise model of the inertial forces leading to particle migration and focusing in curved channels. This is a first attempt to precisely model the complete equations of fluid motion to determine the effect of channel curva-

ture on the inertial forces. Using the full numerical model we observed that particle equilibrium locations are highly dependent on the magnitude of the underlying Dean flow. Based on this full model we have developed a simple perturbation based model that provides a simple yet precise representation of these forces with minimal computation burden. This model proved to be more precise and versatile than the commonly references Stokes model. Future work in this problem will answer the ill-posed inverse problem for which there is no tractable solution *i.e.* can a channel be designed given a desired focusing location? Continued development and investigation of this model can help answer this question and aid in the rapid design of novel biomedical tools.

Chapter 6

Conclusion

Inertial microfluidics is an increasingly growing field and has demonstrated numerous exciting possibilities. This growth is fueled by many transformative uses of inertial flows in biomedicine. These high impact applications include, but certainly not limited to, the isolation of extremely rare cells [40], rapid mechanophenotyping [82], particle fabrication [83].

Although there have been numerous studies on the mechanism of particle inertial microfluidics, and a plethora of applications, precise and rapid design rules are still lacking for particle inertial manipulation in confined geometries. This is largely because inertial microfluidics represents a class of problems that are non-trivial. The physics at hand are described by nonlinear partial differential equations and complicated domains. Existing methods to solve these problems often require time consuming numerical solutions. Consequently, more work is needed to develop better techniques that capture the underlying mechanisms and provide simple tools to users with no expertise of knowledge of fluid mechanics.

In this dissertation I investigated the intricate balance of secondary and inertial forces on particles as a means to precisely manipulate their behavior. The secondary flows (*e.g.* permeate, Dean) serve to adjust the particle equilibrium and trajectories in three-dimensions at high speeds. The effects of these flows can be faithfully reproduced using simple perturbation models that are derived from the underlying physics. Through use of this type of model I showed that the complexity and time required to predict particle

behavior was greatly reduced. While there are a large variety of applications for this tractable forward model, the ultimate goal of this work is to make these results more accessible to researchers with no knowledge of inertial microfluidics. Future work will attempt to integrate some form of machine learning to solve the seemingly intractable reverse problem. That is given a desired focusing location of one or more particles, can we design a channel to achieve this behavior? The relatively new field of inertial microfluidics has only very recently been appreciated as being useful, but with the large amount of interest and the endless applications, inertial microfluidics is well poised to have a large and lasting impact.

Appendix A

A.1 Detailed images of μ-TFF device

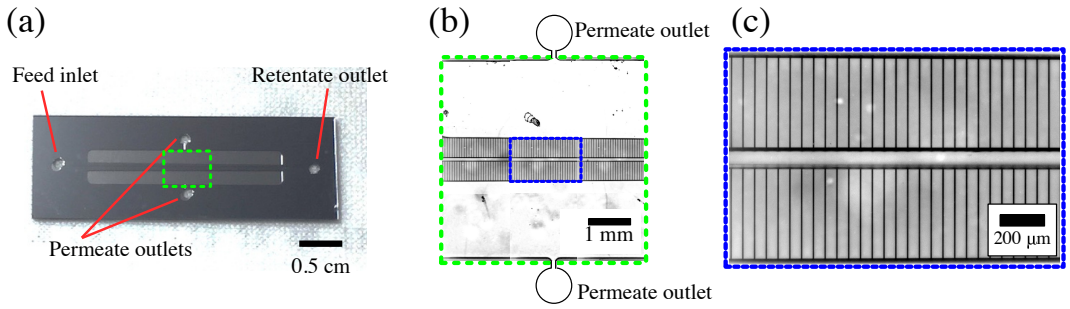

Figure A.1: (a) Image of a microfabricated tangential flow filtration (TFF) device. The image highlights the four channel openings (feed, retentate and permeate) that allow for fluid to be infused and withdrawn from the device. (b) A close-up of the center of the device. The primary channel in the device connects the feed inlet to the retentate outlet, where a portion of the primary flow is diverted to the permeate outlets via the permeate channels. (c) The permeate channels are perpendicular to the primary channel with dimensions of 5 μm by 415 μm long with a spacing between channels of 52.5 μm.

A.2 Equilibrium location as a function of channel Reynolds number in Straight Channel

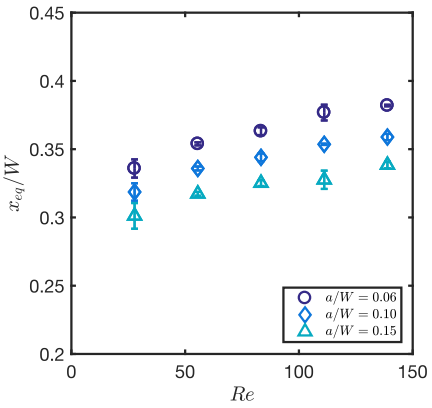

Figure A.2: Equilibrium position of a particle in a straight channel as a function of distance in a straight microchannel (100 x 100 μm) for different Reynolds numbers (Re). These data suggest that the particle location depends very slightly on Reynolds number.

A.3 COMSOL simulations of flow field

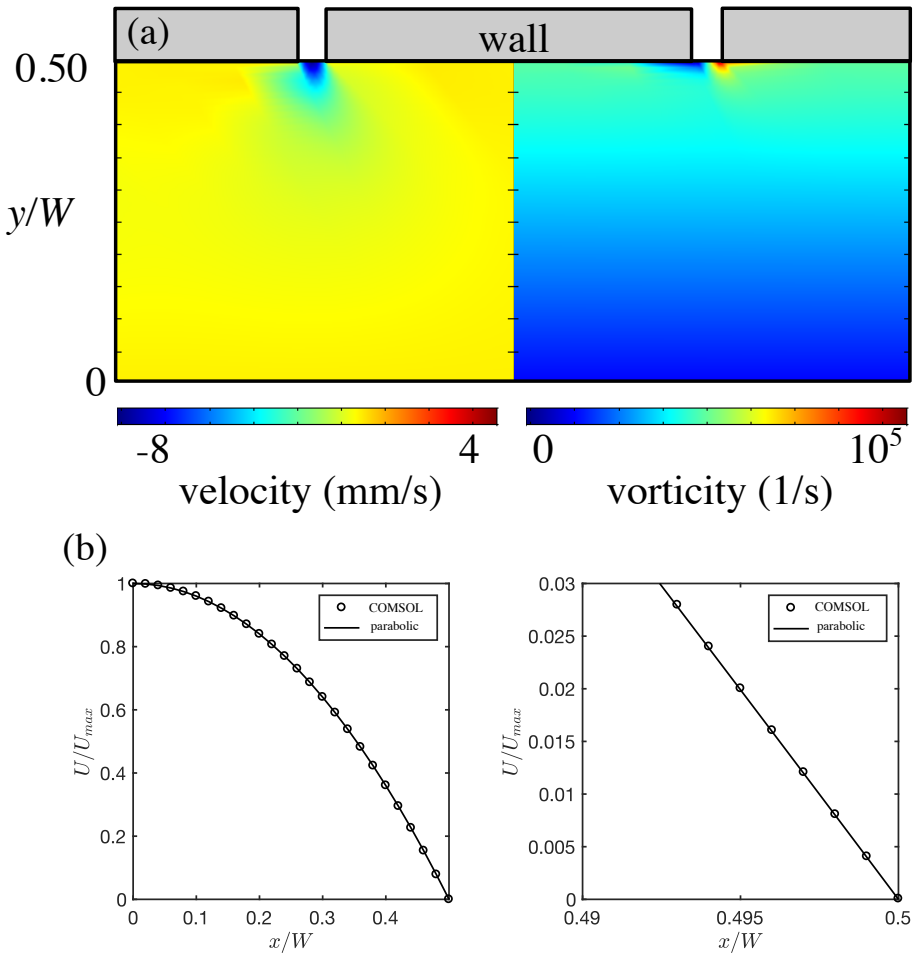

Figure A.3: COMSOL simulation of the flow in a TFF channel at Re =100, y/L = 1 (a) The presence of a transverse permeate flow (and channels) can alter the dynamics of the underlying base flow as characterized by the transverse velocity and vorticity field very close to the permeate channel. (b) Streamwise averaged axial flow profile, showing that the flow field remains unaffected by these localized disturbances.

A.4 Equilibrium location as a function of channel Reynolds number in μ-TFF

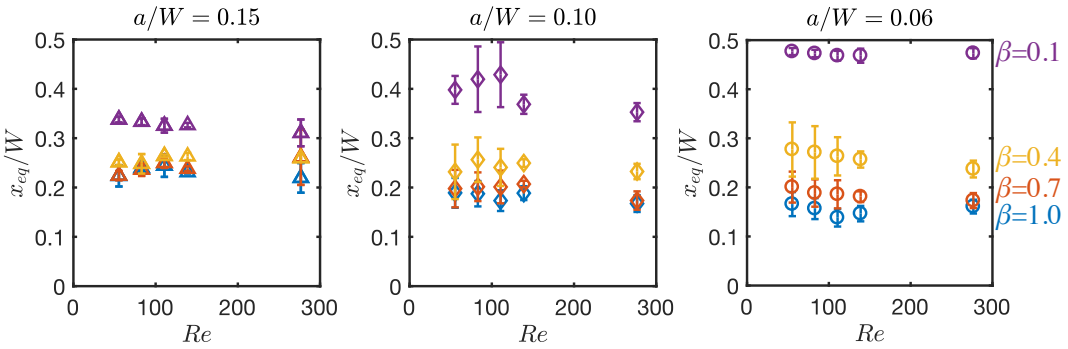

Figure A.4: Experimental measurements of particle stream equilibrium at $(y/L = 1.0)$ over all Reynolds numbers and particle sizes tested. From these data it is apparent that smaller particle sizes are very sensitive to permeate flow and the effects are only slightly dependent on Re.

A.5 Additional momentum term

The momentum equation can be transformed from a velocity field in the lab frame to that of a frame translating with a particle moving at a velocity U_p using the following transformations.

$$t' = t \tag{A.1}$$

$$x'_i = x_i + x_{p,i}(t) \tag{A.2}$$

$$u'_i = u_i + U_{p,i}(t) \tag{A.3}$$

$$p' = p \tag{A.4}$$

Here the variable associated with a prime denote the lab frame and those without a prime denote the moving frame. We can then relate the derivatives with respect to time and space for either frame by:

$$\frac{\partial()}{\partial x_j} = \frac{\partial x'_k}{\partial x_j}\frac{\partial()}{\partial x'_k} = \frac{\partial(x_k + x_{p,k})}{\partial x_j}\frac{\partial()}{\partial x'_k} = \delta_{jk}\frac{\partial()}{\partial x'_k} = \frac{\partial()}{\partial x'_j} \tag{A.5}$$

$$\frac{\partial()}{\partial t} = \frac{\partial t'}{\partial t}\frac{\partial()}{\partial t'} + \frac{\partial x'_k}{\partial t}\frac{\partial()}{\partial x'_k} = \frac{\partial()}{\partial t'} + U_{p,k}\frac{\partial()}{\partial x'_k} \tag{A.6}$$

We can then relate the momentum equation in the lab frame to that of a moving

frame by using equation A.5 & A.5

$$\rho\left[\frac{\partial u_i'}{\partial t'} + u_j'\frac{\partial u_i'}{\partial x_j'}\right] = -\frac{\partial p'}{\partial x_i'} + \mu\frac{\partial}{\partial x_j'}\left(\frac{\partial u_i'}{\partial x_j'}\right) \tag{A.7}$$

$$\rho\left[\frac{\partial (u_i + U_{p,i})}{\partial t'} + (u_j + U_{p,j})\frac{\partial (u_i + U_{p,i})}{\partial x_j'}\right] = -\frac{\partial p}{\partial x_i'} + \mu\frac{\partial}{\partial x_j'}\left(\frac{\partial (u_i + U_{p,i})}{\partial x_j'}\right) \tag{A.8}$$

$$\rho\left[\frac{\partial (u_i + U_{p,i})}{\partial t} - U_{p,j}\frac{\partial (u_i + U_{p,i})}{\partial x_j} + (u_j + U_{p,j})\frac{\partial (u_i + U_{p,i})}{\partial x_j}\right] = -\frac{\partial p}{\partial x_i} + \mu\frac{\partial}{\partial x_j}\left(\frac{\partial (u_i + U_{p,i})}{\partial x_j}\right) \tag{A.9}$$

Now canceling like terms and knowing that $U_{p,i}$ has no spatial gradients because it is only a linear translation of the laboratory frame and not a continuum value, we can write the momentum equation as:

$$\rho\left[\frac{\partial (u_i + U_{p,i})}{\partial t} + u_j\frac{\partial u_i}{\partial x_j}\right] = -\frac{\partial p}{\partial x_i} + \mu\frac{\partial}{\partial x_j}\left(\frac{\partial u_i}{\partial x_j}\right) \tag{A.10}$$

We assume that in the moving reference frame the flow is quasi-steady and thus the time derivative of the flow is zero, yielding:

$$\rho\left[\frac{\partial U_{p,i}}{\partial t} + u_j\frac{\partial u_i}{\partial x_j}\right] = -\frac{\partial p}{\partial x_i} + \mu\frac{\partial}{\partial x_j}\left(\frac{\partial u_i}{\partial x_j}\right) \tag{A.11}$$

At a given moment in time the acceleration of the particle that is being tracked by the moving reference frame is dictated by the underlying flow ($\bar{u}_i$) and its gradient and

thus the acceleration is given by

$$\frac{\partial U_{p,i}}{\partial t} = U_{p,j}\frac{\partial \bar{u}_i}{\partial x_j} \tag{A.12}$$

Finally, substituting this term back into the momentum equation yields:

$$\rho\left[U_{p,j}\frac{\partial \bar{u}_i}{\partial x_j} + u_j\frac{\partial u_i}{\partial x_j}\right] = -\frac{\partial p}{\partial x_i} + \mu\frac{\partial}{\partial x_j}\left(\frac{\partial u_i}{\partial x_j}\right) \tag{A.13}$$

where $\bar{u}$ is the undisturbed velocity field. However, the only non-zero component of (A12) in our model acts in the axial direction and scales with γ as:

$$\frac{\partial U_{p,i}}{\partial t} = U_{p,j}\frac{\partial \bar{u}_i}{\partial x_j} \sim U_p\frac{\gamma U}{W} \tag{A.14}$$

Note the term is negligible for small γ and near the channel walls where U_p approaches zero.

A.6 Correction to Stokes' drag and the relationship to g

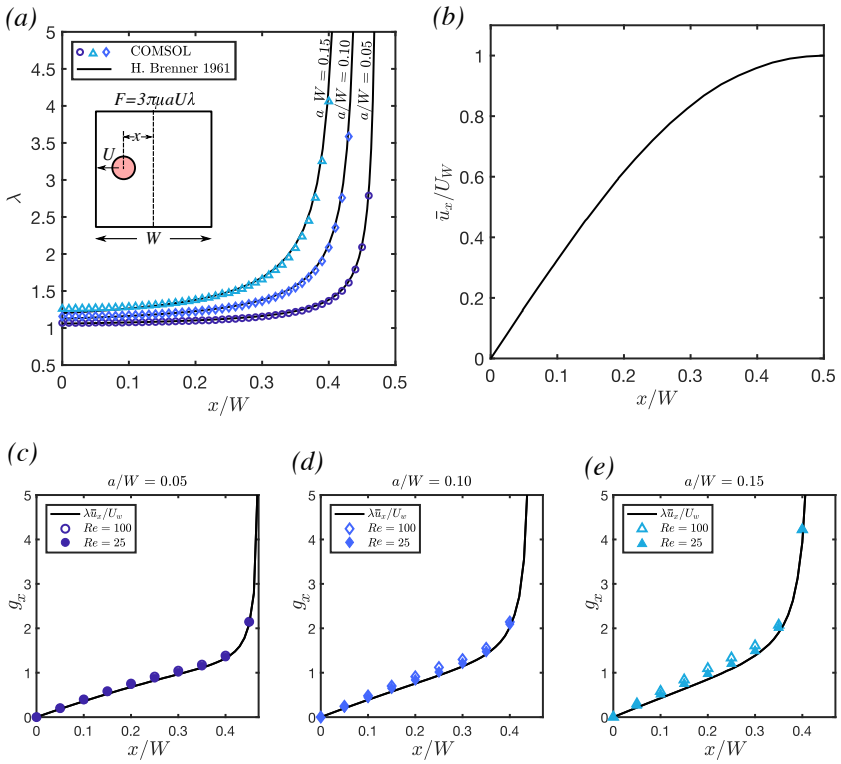

Figure A.5: (a) The relationship between the translational velocity of a sphere (U) and the force (F) required to produce such a motion can be significantly modified by the effects of confining walls. We show the effect of this spatial retardation (λ) on spheres of diameter $a/W = 0.05, 0.10, 0.15$ (at $z/W = 0$) and compare with the analytic results of [4]. (b) A plot of the spatially varying permeate velocity (at $z/W = 0$) within the channel modeled in this work. At the walls the permeate velocity is maximal ($u_x/U_W = 1$) and decays to zero at the center of the channel. (c) Normalized residual curves (g_x) as a function of x/W at $z/W = 0$ for a particle of diameter $a/W = 0.05$ (d) Normalized residual curves (g_x) as a function of x/W at $z/W = 0$ for a particle of diameter $a/W = 0.10$ (e) Normalized residual curves (g_x) as a function of x/W at $z/W = 0$ for a particle of diameter $a/W = 0.15$ The solid black lines in (c)-(e) represent g_x modeled using the retardation factor and permeate velocity depicted in (a) and (b) respectively.

When the size of a flowing particle is comparable to the dimensions of its confining channel, it is important to consider the hydrodynamic effects from the walls on the lateral

motion of the particle. To account for this, we introduce a spatially varying retardation factor λ that relates force (F) on a particle of diameter (a) and its migration velocity (U) [4]:

$$F = 3\pi\mu a U\lambda \tag{A.15}$$

Here, λ is calculated with a numerical simulation where a particle is modeled in a square channel of cross-section $W \times W$ and is assigned a velocity U ($Re \ll 1$) in the direction of a wall. Then we calculate the required force to produce such a motion by integrating the fluid stress on the surface of the particle and using equation A.15 we solve for λ. We repeat this process for discrete locations that span the width of the channel. In figure 9a we plot λ for three particles ($a/W = 0.05, 0.10, 0.15$ at $z/W = 0$) and show how our calculations compare to the existing analytic model [4]. Interestingly, even though in our simulations the particle is confined by four walls, the semi-infinite domain of the Brenner model seems to match well at $z/W = 0$. In our work we find that the normalized residual $\boldsymbol{g}$ (figure 4.4b & 4.4c) is weakly dependent on Re. A quick approximation of $\boldsymbol{g}$ (for any sized particle) may useful for any researcher who may be interested in applying this linear model. Here we provide a simple method for approximating $\boldsymbol{g}$. We begin by interpreting $\boldsymbol{g}$ to represent the effects of the permeate flow (U_W) on the force ($\mathbf{F}_P$) experienced by a particle.

$$\mathbf{F}_P = \gamma\mathbf{F}_1 = 3\pi\mu a U_W \boldsymbol{g} \tag{A.16}$$

Likewise, if we interpret equation A.15 as the force experienced by particle with a flow moving past it (*i.e.* particle reference frame) then we can construct a force field everywhere in the channel according to the local permeate velocity given by the x, and

z components of undisturbed flow $\bar{\mathbf{u}}$ that should approximate the permeate force field.

$$\mathbf{F}_p \approx 3\pi\mu a\bar{\mathbf{u}}\lambda \tag{A.17}$$

Without loss of generality we consider only the x-component of the permeate force. If we equate equation A.16 and A.17 to obtain a relationship for g_x:

$$g_x \approx \lambda\frac{\bar{u}_x}{U_W} \tag{A.18}$$

Here $\bar{u}_x$ is x-component of the undisturbed flow and can be seen in figure 9b. The results of implementing equation A.18 can be seen in figures A.5c-e. Where in general the approximation works best for smaller particles at a lower Re. However, the approximation is remarkably accurate and only requires knowledge of flow field, which is relatively simple to determine.

A.7 Local volumetric flow rate in a porous channel

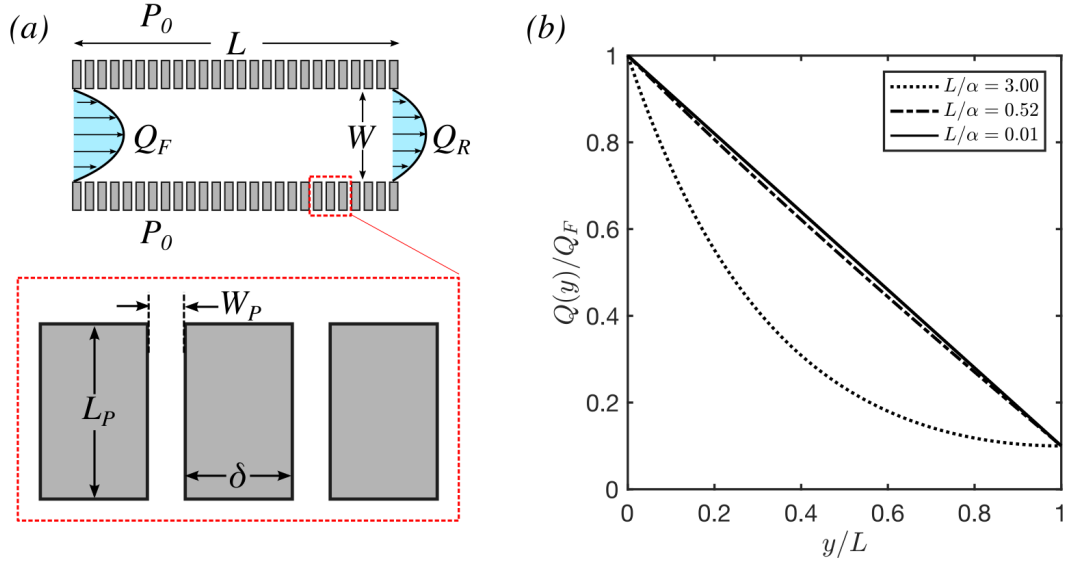

Figure A.6: (a) schematic showing the microfluidic device used in the experiments. The channel has a height W into the page (b) volumetric flow rate curves for channels of varying channel resistance L/δ ($\delta^2 = R_P/R_C$) for a $\beta = 0.1$ ($\beta = Q_R/Q_F$) as L/δ approaches 0 the axial flowrate distribution becomes linear.

The local volumetric flow rate in a porous duct $Q(y)$ is typically axially varying due to a non-zero fluid flux. Thus the local volumetric flow rate can be modeled as:

$$Q(y) = Q_F - \int_0^y U_W(y')\, W dy' \tag{A.19}$$

Where Q_F is the feed flow rate (*i.e.*, $Q(y = 0)$), U_W is the average permeate flow velocity, W is the channel height and y is the axial coordinate. Now assuming that the wall can be treated as a continuously porous wall of a constant permeability we can use Darcy's law to write.

$$Q(y) = Q_F - \int_0^y \kappa \frac{P(y') - P_0}{\mu L_P}\, W dy' \tag{A.20}$$

Where $P(y')$ is the local pressure in the channel, P_0 is the reservoir pressure on the

other side of porous wall, L_p is the wall thickness and κ is the wall permeability. It is convenient to define the constant $R_P = \mu L_P/\kappa W$ so that we can rewrite equation A.20

$$Q(y) = Q_F - \int_0^y \frac{P(y') - P_0}{R_P}\, dy' \tag{A.21}$$

Equation A.21 can be rewritten in terms of pressure by using the Hagen-Poiseuille equation:

$$Q = -\frac{1}{R_C}\frac{dP}{dy} \tag{A.22}$$

Here R_C represents the channel resistance per unit length in the axial direction. This equation can now be substituted into A.21

$$-\frac{1}{R_C}\frac{dP}{dy} = Q_F - \int_0^y \frac{P(y') - P_0}{R_P}\, dy' \tag{A.23}$$

If we differentiate equation A.23 once and use the fundamental theorem of calculus we obtain a ordinary differential equation for the axial pressure distribution.

$$-\frac{1}{R_C}\frac{d^2P}{dy^2} = -\frac{P(y) - P_0}{R_P} \tag{A.24}$$

Now rearranging the equation to a standard form

$$\frac{R_P}{R_C}\frac{d^2P}{dy^2} - P(y) + P_0 = 0 \tag{A.25}$$

say that $\delta^2 = R_P/R_C$ and solve the ODE

$$P(y) = C_1 \exp\left(\frac{y}{\delta}\right) + C_2 \exp\left(\frac{-y}{\delta}\right) + P_0 \tag{A.26}$$

This solution is valid however the known boundary conditions are in terms of volu-

metric flowrate. Therefore, it is convenient to differentiate the solution once

$$\frac{dP}{dy} = \frac{C_2}{\delta}\exp\left(\frac{-y}{\delta}\right) - \frac{C_1}{\delta}\exp\left(\frac{y}{\delta}\right) \tag{A.27}$$

and then again apply the Hagen-Poiseuille relationship to obtain the axial flowrate distribution

$$Q(y) = \frac{C_1}{\delta R_C}\exp\left(\frac{y}{\delta}\right) - \frac{C_2}{\delta R_C}\exp\left(\frac{-y}{\delta}\right) \tag{A.28}$$

Where the boundary conditions are $Q(0) = Q_F$ and $Q(L) = Q_R$ and are used to solve for C_1 and C_2

$$C_1 = \frac{-\delta R_C \exp\left(\frac{L}{\delta}\right)\left[Q_R - Q_F \exp\left(\frac{-L}{\delta}\right)\right]}{\exp\left(\frac{2L}{\delta}\right) - 1} \tag{A.29}$$

and

$$C_2 = \frac{-\delta R_C \exp\left(\frac{L}{\delta}\right)\left[Q_R - Q_F \exp\left(\frac{L}{\delta}\right)\right]}{\exp\left(\frac{2L}{\delta}\right) - 1} \tag{A.30}$$

upon simplification

$$Q(y) = \frac{Q_R \sinh\left(\frac{y}{\delta}\right) + Q_F \sinh\left(\frac{L-y}{\delta}\right)}{\sinh\left(\frac{L}{\delta}\right)} \tag{A.31}$$

This model is sufficient to model the flow rate in a porous channel, but it can be further simplified in the limit where the flow resistance through the channel wall is much greater than the resistance through the primary channel $L/\delta << 1$ and $\sinh(L/\delta) \approx L/\delta$ and in this limit equation A.31 reduces down to

$$Q(y) = Q_F\left[1 + \frac{y}{L}(\beta - 1)\right] \quad and \quad \beta = Q_R/Q_F \tag{A.32}$$

The resistance of a rectangular section of channel of height $2b$ and width $2a$ ($a > b$) is given by [61].

$$R = \frac{3\mu}{4ba^3\left(1 - \frac{192a}{\pi^5 b}\sum_{n=1,3,5,\ldots}^{\infty}\frac{\tanh(n\pi b/2a)}{n^5}\right)} \tag{A.33}$$

For a square channel of width, W height, W the axial channel resistance is given by

$$R_C \approx \frac{28\mu}{W^4} \tag{A.34}$$

The permeability of a porous material is defined as

$$\kappa = \mu\bar{U}\frac{L_p}{\Delta P} \tag{A.35}$$

choosing the right formulation for average permeate velocity $\bar{U}_W$ is not obvious, but one reasonable approximation is to treat the wall as a continuously permeable (rather than discretely) but then use the resistance of single permeate channel to calculate the volumetric flow rate for a section of the channel.

$$Q = 2\bar{U}_W W(W_P + \delta) = \left[1 - \frac{192W}{\pi^5 W_p}\sum_{n=1,3,5,\ldots}^{\infty}\frac{\tanh(n\pi W_p/2W)}{n^5}\right]\frac{W^3 W_P}{12\mu}\frac{\Delta P}{L_p} \tag{A.36}$$

Equation A.35 can be used to solve for an expression giving $\bar{U}_W$. Here $\Delta P = P(y) - P_0$ and W_P is the width of the permeate channels (figure A.6). Knowing $\bar{U}_W$ we can substitute that into the definition of κ (equation A.34) then substitute κ into the definition of R_P to arrive at:

$$R_P \approx \frac{24\mu L_P(W_p + \delta)}{W^3 W_P[1 - 0.63(W/W_P)\tanh(\pi W_p/2W)]} \tag{A.37}$$

If we use values that are representative of our microchannel we can calculate a value of $\delta \approx 0.0194\,\mathrm{m}$ and the resulting ratio $L/\delta = 0.52$. This ratio is of $\mathcal{O}(10^{-1})$ which is sufficiently small to use the small angle approximation that results in the distribution of equation A.32. Figure A.6b shows that as L/δ decreases we observe a more linear trend in the axial flowrate distribution and for $L/\delta = 0.01$ the distribution is for all practical purposes linear which is approximated well by $L/\delta = 0.52$.

A.8 Quasi-Steady Assumption

In the numerical models presented in this dissertation we consider a particle that is moving at a velocity U_p such that it experiences no net force in the streamwise direction (and no torque). This formulation of the problem is a quasi-steady approach that implies that the particle migrates across streamlines so slowly that there is no time dependence in the equations of motion. In general, the equations of motion should reflect a balance between the particles drag and inertial forces.

$$m_p \frac{d}{dt}\big(U_p \mathbf{e}_y\big) = \mathbf{e}_y \cdot \int_s \mathbf{n_r} \cdot \mathbf{T}\, ds \tag{A.38}$$

Here we assume $\mathbf{e}_y$ is the streamwise direction, U_p is the particles velocity, m_p is the mass of the particle, $\mathbf{T}$ is the total stress tensor, and $\mathbf{n}_r$ is the unit normal on the surface of the sphere. To validate our force free assumption, we non-dimensionalize equation A.38 using the characteristic scales associated with each variable. That is:

$$U_p' = \frac{U_p}{U}, \quad t' = \frac{t}{\tau}, \quad \mathbf{T}' = \frac{\mathbf{T}}{(\mu U/a)}, \quad ds' = \frac{ds}{a^2} \tag{A.39}$$

Where U is average flow velocity, τ is the characteristic timescale of the lateral migration, a is the particles diameter, and μ is the fluid viscosity. To determine this timescale, we consider the particles lateral migration as it moves through the flow. The timescale of this movement is given by:

$$\tau \sim \frac{W}{U_{mig}} \tag{A.40}$$

If we assume that force causing the lateral migration of the particle scales as $F_L \sim \rho U^2 a^4/W^2$ where ρ is the fluid (and particle) density, and W is the channel width, then we can estimate the migration velocity by balancing this force with a viscous drag

$(F \sim \mu a U_{mig})$:

$$U_{mig} = \frac{\rho U^2 a^4 / W^2}{\mu a} \tag{A.41}$$

Finally we can non-dimensionalize equation A.38 using equation A.39, A.40 and A.41:

$$Re_p^2 \left(\frac{a}{W} \right) \frac{d}{dt'} \left(U_p' \mathbf{e}_y \right) = \mathbf{e}_y \cdot \int_s \mathbf{n_r} \cdot \mathbf{T}' \, ds' \tag{A.42}$$

Here Re_p is the particle Reynolds number and is defined as $Re_p = \frac{\rho U W}{\mu} \left(\frac{a}{w} \right)^2$. From equation A.42 it is apparent that because of the $\mathcal{O}(Re)$ migration experiences translational acceleration that are $\mathcal{O}(Re^2)$. The force free assumption becomes questionable at large values of $Re_p^2 \left(\frac{a}{w} \right)$. However, in the model presented in this dissertation this parameter is small enough ($\mathcal{O}(0.1)$ at the most extreme case) that the acceleration of the particle can be neglected and the force free assumption is valid. Note that a similar non-dimensionalization can be done for rotational equations of motion, where the result is:

$$Re_p^2 \left(\frac{a}{W} \right)^2 \frac{d\mathbf{\Omega}'}{dt'} = \int_s \mathbf{n_r} \cdot \left(\mathbf{r}' \times \mathbf{T}' \right) ds' \tag{A.43}$$

Here $\mathbf{\Omega'}$ is the particle's rotation rate non-dimensionalized by the flow times scale U/W and $\mathbf{r}$' is the position vector normalized by the particle diameter. The inertial terms on left hand side of equation A.43 are more stringent than in equation A.42 and therefore, the particle can also be modeled as torque free.

Bibliography

[1] D. Di Carlo, J. F. Edd, K. J. Humphry, H. A. Stone, and M. Toner, "Particle Segregation and Dynamics in Confined Flows," *Physical Review Letters*, vol. 102, no. 9, p. 094503, (2009).

[2] M. Garcia and S. Pennathur, "Inertial particle dynamics in the presence of a secondary flow," *Physical Review Fluids*, vol. 2, no. 4, p. 042201, (2017).

[3] J. M. Martel and M. Toner, "Particle Focusing in Curved Microfluidic Channels," *Scientific Reports*, vol. 3, p. 3340, Nov. (2013).

[4] H. Brenner, "The slow motion of a sphere through a viscous fluid towards a plane surface," *Chemical Engineering Science*, vol. 16, no. 3-4, pp. 242–251, (1961).

[5] A. Gross, J. Schoendube, S. Zimmermann, M. Steeb, R. Zengerle, and P. Koltay, "Technologies for Single-Cell Isolation," *International Journal of Molecular Sciences*, vol. 16, no. 8, pp. 16897–16919, (2015).

[6] R. Rosenberg, R. Gertler, J. Friederichs, K. Fuehrer, M. Dahm, R. Phelps, S. Thorban, H. Nekarda, and J. R. Siewert, "Comparison of two density gradient centrifugation systems for the enrichment of disseminated tumor cells in blood," *Cytometry*, vol. 49, no. 4, pp. 150–158, (2002).

[7] H. Ramachandraiah, H. A. Svahn, and A. Russom, "Inertial microfluidics combined with selective cell lysis for high throughput separation of nucleated cells from whole blood," *RSC Advances*, vol. 7, no. 47, pp. 29505–29514, (2017).

[8] C. Wyatt Shields IV, C. D. Reyes, and G. P. Lopez, "Microfluidic cell sorting: a review of the advances in the separation of cells from debulking to rare cell isolation," *Lab Chip*, vol. 15, pp. 1230–1249, (2015).

[9] Y. Yoon, S. Kim, J. Lee, J. Choi, R.-K. Kim, S.-J. Lee, O. Sul, and S.-B. Lee, "Clogging-free microfluidics for continuous size-based separation of microparticles," *Scientific Reports*, vol. 6, no. 1, p. 26531, (2016).

[10] M. Pødenphant, N. Ashley, K. Koprowska, K. U. Mir, M. Zalkovskij, B. Bilenberg, W. Bodmer, A. Kristensen, and R. Marie, "Separation of cancer cells from white

blood cells by pinched flow fractionation," *Lab on a Chip*, vol. 15, no. 24, pp. 4598–4606, (2015).

[11] S. Ranjan, K. K. Zeming, R. Jureen, D. Fisher, and Y. Zhang, "DLD pillar shape design for efficient separation of spherical and non-spherical bioparticles," *Lab on a Chip*, vol. 14, no. 21, pp. 4250–4262, (2014).

[12] P. Sajeesh and A. K. Sen, "Particle separation and sorting in microfluidic devices: a review," *Microfluidics and Nanofluidics*, vol. 17, no. 1, pp. 1–52, (2014).

[13] H. Tsutsui and C.-M. Ho, "Cell separation by non-inertial force fields in microfluidic systems," *Mechanics Research Communications*, vol. 36, no. 1, pp. 92–103, (2009).

[14] D. Di Carlo, D. Irimia, R. G. Tompkins, and M. Toner, "Continuous inertial focusing, ordering, and separation of particles in microchannels," *Proceedings of the National Academy of Sciences*, vol. 104, no. 48, pp. 18892–18897, (2007).

[15] D. Di Carlo, "Inertial microfluidics," *Lab on a Chip*, vol. 9, no. 21, pp. 3038–3046, (2009).

[16] M. E. Warkiani, L. Wu, A. K. P. Tay, and J. Han, "Large-Volume Microfluidic Cell Sorting for Biomedical Applications," *Annual Review of Biomedical Engineering*, vol. 17, no. 1, pp. 1–34, (2015).

[17] J. Zhang, S. Yan, D. Yuan, G. Alici, N.-T. Nguyen, M. E. Warkiani, and W. Li, "Fundamentals and applications of inertial microfluidics: a review," *Lab on a Chip*, vol. 16, no. 1, pp. 10–34, (2016).

[18] G. Segré and A. Silberberg, "Radial Particle Displacements in Poiseuille Flow of Suspensions," *Nature*, vol. 189, no. 4760, pp. 209–210, (1961).

[19] B. P. Ho and L. G. Leal, "Inertial migration of rigid spheres in two-dimensional unidirectional flows," *Journal of Fluid Mechanics*, vol. 65, no. 2, pp. 365–400, (1974).

[20] J. A. Schonberg and E. J. Hinch, "Inertial migration of a sphere in Poiseuille flow," *Journal of Fluid Mechanics*, vol. 203, pp. 517–524, (1989).

[21] E. S. Asmolov, "The inertial lift on a spherical particle in a plane Poiseuille flow at large channel Reynolds number," *Journal of Fluid Mechanics*, vol. 381, pp. 63–87, (1999).

[22] K. Hood, S. Lee, and M. Roper, "Inertial migration of a rigid sphere in three-dimensional Poiseuille flow," *Journal of Fluid Mechanics*, vol. 765, pp. 452–479, (2015).

[23] A. Sarkar, H. W. Hou, A. E. Mahan, J. Han, and G. Alter, "Multiplexed Affinity-Based Separation of Proteins and Cells Using Inertial Microfluidics," *Scientific Reports*, vol. 6, no. 1, p. 23589, (2016).

[24] J. Zhang, S. Yan, R. Sluyter, W. Li, G. Alici, and N.-T. Nguyen, "Inertial particle separation by differential equilibrium positions in a symmetrical serpentine microchannel," *Scientific Reports*, vol. 4, p. 4527, Mar. 2014.

[25] A. J. Mach and D. Di Carlo, "Continuous scalable blood filtration device using inertial microfluidics," *Biotechnology and Bioengineering*, vol. 107, no. 2, pp. 302–311, (2010).

[26] J. M. Martel, K. C. Smith, M. Dlamini, K. Pletcher, J. Yang, M. Karabacak, D. A. Haber, R. Kapur, and M. Toner, "Continuous Flow Microfluidic Bioparticle Concentrator," *Scientific Reports*, vol. 5, no. 1, p. 11300, (2015).

[27] S. S. Kuntaegowdanahalli, A. A. S. Bhagat, G. Kumar, and I. Papautsky, "Inertial microfluidics for continuous particle separation in spiral microchannels," *Lab on a Chip*, vol. 9, no. 20, pp. 2973–2980, (2009).

[28] A. Pabby, S. Rizvi, and A. Requena, eds., *Handbook of Membrane Separations*. Chemical, Pharmaceutical, Food, and Biotechnological Applications, Second Edition, CRC Press, (2015).

[29] G. Belfort, R. H. Davis, and A. L. Zydney, "The behavior of suspensions and macromolecular solutions in crossflow microfiltration," *Journal of Membrane Science*, vol. 96, no. 1-2, pp. 1–58, (1994).

[30] M. Kim and A. Zydney, "Theoretical analysis of particle trajectories and sieving in a two-dimensional cross-flow filtration system," *Journal of Membrane Science*, vol. 281, no. 1-2, pp. 666–675, (2006).

[31] A. M. C. van Dinther, C. G. P. H. Schroën, and R. M. Boom, "High-flux membrane separation using fluid skimming dominated convective fluid flow," *Journal of Membrane Science*, vol. 371, no. 1-2, pp. 20–27, (2011).

[32] F. W. Altena and G. Belfort, "Lateral migration of spherical particles in porous flow channels: application to membrane filtration," *Chemical Engineering Science*, vol. 39, no. 2, pp. 343–355, (1984).

[33] J. R. Otis, F. W. Altena, J. T. Mahar, and G. Belfort, "Measurements of single spherical particle trajectories with lateral migration in a slit with one porous wall under laminar flow conditions," *Experiments in Fluids*, vol. 4, no. 1, pp. 1–10, (1986).

[34] K. Hood, S. Kahkeshani, D. Di Carlo, and M. Roper, "Direct measurement of particle inertial migration in rectangular microchannels," *Lab on a Chip*, vol. 16, no. 15, pp. 2840–2850, (2016).

[35] J. Zhou and I. Papautsky, "Fundamentals of inertial focusing in microchannels," *Lab on a Chip*, vol. 13, no. 6, pp. 1121–1132, (2013).

[36] S. M. Ranuncolo, "Liquid Biopsy in Liquid Tumors," *Journal of Cancer Therapy*, vol. 08, no. 03, pp. 302–320, (2017).

[37] V. Gupta, I. Jafferji, M. Garza, V. O. Melnikova, D. K. Hasegawa, R. Pethig, and D. W. Davis, "ApoStream^{TM}, a new dielectrophoretic device for antibody independent isolation and recovery of viable cancer cells from blood," *Biomicrofluidics*, vol. 6, no. 2, p. 024133, (2012).

[38] P. Augustsson, C. Magnusson, M. Nordin, H. Lilja, and T. Laurell, "Microfluidic, Label-Free Enrichment of Prostate Cancer Cells in Blood Based on Acoustophoresis," *Analytical Chemistry*, vol. 84, no. 18, pp. 7954–7962, (2012).

[39] G. Vona, A. Sabile, M. Louha, V. Sitruk, S. Romana, K. Schütze, F. Capron, D. Franco, M. Pazzagli, M. Vekemans, B. Lacour, C. Bréchot, and P. Paterlini-Bréchot, "Isolation by Size of Epithelial Tumor Cells: A New Method for the Immunomorphological and Molecular Characterization of Circulating Tumor Cells," *The American Journal of Pathology*, vol. 156, no. 1, pp. 57–63, (2000).

[40] E. Sollier, D. E. Go, J. Che, D. R. Gossett, S. O'Byrne, W. M. Weaver, N. Kummer, M. Rettig, J. Goldman, N. Nickols, S. McCloskey, R. P. Kulkarni, and D. Di Carlo, "Size-selective collection of circulating tumor cells using Vortex technology," *Lab on a Chip*, vol. 14, no. 1, pp. 63–77, (2014).

[41] P. Hadikhani, S. M. H. Hashemi, G. Balestra, L. Zhu, M. A. Modestino, F. Gallaire, and D. Psaltis, "Inertial manipulation of bubbles in rectangular microfluidic channels," *Lab on a Chip*, vol. 18, no. 7, pp. 1035–1046, (2018).

[42] C. K. W. Tam and W. A. Hyman, "Transverse motion of an elastic sphere in a shear field," *Journal of Fluid Mechanics*, vol. 59, no. 1, pp. 177–185, (1973).

[43] S. C. Hur, N. K. Henderson-MacLennan, E. R. B. McCabe, and D. Di Carlo, "Deformability-based cell classification and enrichment using inertial microfluidics," *Lab on a Chip*, vol. 11, no. 5, pp. 912–920, (2011).

[44] R. G. Cox and H. Brenner, "The lateral migration of solid particles in Poiseuille flow — I theory," *Chemical Engineering Science*, vol. 23, no. 2, pp. 147–173, (1968).

[45] P. G. Saffman, "The lift on a small sphere in a slow shear flow," *Journal of Fluid Mechanics*, vol. 22, no. 2, pp. 385–400, (1965).

[46] J. M. Martel and M. Toner, "Inertial Focusing in Microfluidics," *Annual Review of Biomedical Engineering*, vol. 16, no. 1, pp. 371–396, (2014).

[47] H. Amini, W. Lee, and D. Di Carlo, "Inertial microfluidic physics," *Lab on a Chip*, vol. 14, no. 15, pp. 2739–2761, (2014).

[48] I.-S. Chang and S.-N. Kim, "Wastewater treatment using membrane filtration—effect of biosolids concentration on cake resistance," *Process Biochemistry*, vol. 40, no. 3-4, pp. 1307–1314, (2005).

[49] L. Fernández García, S. Álvarez Blanco, and F. A. Riera Rodríguez, "Microfiltration applied to dairy streams: removal of bacteria," *Journal of the Science of Food and Agriculture*, vol. 93, no. 2, pp. 187–196, (2013).

[50] Pall Corporation, "Breweries using Pall's Keraflux™ Tangential Flow Filtration (TFF) technology increase yield and reduce waste streams," pp. 1–2, (2015).

[51] A. F. Palmer, G. Sun, and D. R. Harris, "Tangential flow filtration of hemoglobin," *Biotechnology Progress*, vol. 25, no. 1, pp. 189–199, (2009).

[52] C. Charcosset, "Membrane processes in biotechnology: An overview," *Biotechnology Advances*, vol. 24, no. 5, pp. 482–492, (2006).

[53] B. Chun and A. J. C. Ladd, "Inertial migration of neutrally buoyant particles in a square duct: An investigation of multiple equilibrium positions," *Physics of Fluids*, vol. 18, no. 3, p. 031704, (2006).

[54] C. Liu, G. Hu, X. Jiang, and J. Sun, "Inertial focusing of spherical particles in rectangular microchannels over a wide range of Reynolds numbers," *Lab on a Chip*, vol. 15, no. 4, pp. 1168–1177, (2015).

[55] D. A. Drew, J. A. Schonberg, and G. Belfort, "Lateral inertial migration of a small sphere in fast laminar flow through a membrane duct," *Chemical Engineering Science*, vol. 46, no. 12, pp. 3219–3224, (1991).

[56] N. A. Lebedeva and E. S. Asmolov, "Migration of settling particles in a horizontal viscous flow through a vertical slot with porous walls," *International Journal of Multiphase Flow*, vol. 37, no. 5, pp. 453–461, (2011).

[57] J. Kim, J. Lee, C. Wu, S. Nam, D. Di Carlo, and W. Lee, "Inertial focusing in non-rectangular cross-section microchannels and manipulation of accessible focusing positions," *Lab on a Chip*, vol. 16, no. 6, pp. 992–1001, (2016).

[58] D. R. Gossett, H. T. K. Tse, J. S. Dudani, K. Goda, T. A. Woods, S. W. Graves, and D. Di Carlo, "Inertial Manipulation and Transfer of Microparticles Across Laminar Fluid Streams," *Small*, vol. 8, no. 17, pp. 2757–2764, (2012).

[59] K. Miura, T. Itano, and M. Sugihara-Seki, "Inertial migration of neutrally buoyant spheres in a pressure-driven flow through square channels," *Journal of Fluid Mechanics*, vol. 749, pp. 320–330, (2014).

[60] H. Shichi, H. Yamashita, J. Seki, T. Itano, and M. Sugihara-Seki, "Inertial migration regimes of spherical particles suspended in square tube flows," *Physical Review Fluids*, vol. 2, no. 4, p. 044201, (2017).

[61] F. M. White, *Viscous fluid flow*. McGraw Hill, second edition ed., (2006).

[62] S. S. P. Nathamgari, B. Dong, F. Zhou, W. Kang, J. P. Giraldo-Vela, T. McGuire, R. L. McNaughton, C. Sun, J. A. Kessler, and H. D. Espinosa, "Isolating single cells in a neurosphere assay using inertial microfluidics," *Lab on a Chip*, vol. 15, no. 24, pp. 4591–4597, (2015).

[63] D. R. Gossett and D. Di Carlo, "Particle Focusing Mechanisms in Curving Confined Flows," *Analytical Chemistry*, vol. 81, no. 20, pp. 8459–8465, (2009).

[64] L. Wang and D. S. Dandy, "High-Throughput Inertial Focusing of Micrometer- and Sub-Micrometer-Sized Particles Separation," *Advanced Science*, vol. 4, no. 10, p. 1700153, (2017).

[65] N. Nivedita, P. Ligrani, and I. Papautsky, "Dean Flow Dynamics in Low-Aspect Ratio Spiral Microchannels," *Scientific Reports*, vol. 7, no. 1, p. 44072, (2017).

[66] M. Norouzi and N. Biglari, "An analytical solution for Dean flow in curved ducts with rectangular cross section," *Physics of Fluids*, vol. 25, no. 5, p. 053602, (2013).

[67] W. D. M.A., "Xvi. note on the motion of fluid in a curved pipe," *The London, Edinburgh, and Dublin Philosophical Magazine and Journal of Science*, vol. 4, no. 20, pp. 208–223, (1927).

[68] A. Özbey, M. Karimzadehkhouei, S. Akgönül, D. Gozuacik, and A. Koşar, "Inertial Focusing of Microparticles in Curvilinear Microchannels," *Scientific Reports*, vol. 6, p. 38809, Dec. (2016).

[69] D. J. Lee, H. Brenner, J. R. Youn, and Y. S. Song, "Multiplex Particle Focusing via Hydrodynamic Force in Viscoelastic Fluids," *Scientific Reports*, vol. 3, no. 1, p. 3258, (2013).

[70] A. A. S. Bhagat, S. S. Kuntaegowdanahalli, and I. Papautsky, "Continuous particle separation in spiral microchannels using dean flows and differential migration," *Lab on a Chip*, vol. 8, no. 11, pp. 1906–1914, (2008).

[71] E. Pedrol, J. Massons, F. Díaz, and M. Aguiló, "Two-Way Coupling FSI Approach to Inertial Focusing Dynamics Under Dean Flow Patterns in Asymmetric Serpentines," *preprints.org*, (2018).

[72] C. Yuan, Z. Pan, and H. Wu, "Inertial migration of single particle in a square microchannel over wide ranges of Re and particle sizes," *Microfluidics and Nanofluidics*, vol. 22, no. 9, p. 102, (2018).

[73] J. Zhang, W. Li, M. Li, G. Alici, and N.-T. Nguyen, "Particle inertial focusing and its mechanism in a serpentine microchannel," *Microfluidics and Nanofluidics*, vol. 17, no. 2, pp. 305–316, (2014).

[74] R. Rasooli and B. Çetin, "Assessment of Lagrangian Modeling of Particle Motion in a Spiral Microchannel for Inertial Microfluidics," *Micromachines*, vol. 9, no. 9, p. 433, (2018).

[75] J. M. Martel, M. Toner, N. Elabbasi, D. Quinn, and J. Bergstorm, "Modeling inertial focusing in straight and curved microfluidic channels," *COMSOL News*, (2013).

[76] A. Dinler and I. Okumus, "Inertial particle separation in curved networks: A numerical study," *Chemical Engineering Science*, vol. 182, pp. 119–131, (2018).

[77] E. E. Michaelides, "Review—The Transient Equation of Motion for Particles, Bubbles, and Droplets," *Journal of Fluids Engineering*, vol. 119, no. 2, pp. 233–247, 1997.

[78] M. R. Maxey and J. J. Riley, "Equation of motion for a small rigid sphere in a nonuniform flow," *The Physics of Fluids*, vol. 26, no. 4, p. 883, (1983).

[79] M. R. Maxey and J. J. Riley, "Equation of motion for a small rigid sphere in a nonuniform flow," *The Physics of Fluids*, vol. 26, p. 883, Sept. 1998.

[80] D. S. W. Lim, J. P. Shelby, J. S. Kuo, and D. T. Chiu, "Dynamic formation of ring-shaped patterns of colloidal particles in microfluidic systems," *Applied Physics Letters*, vol. 83, no. 6, pp. 1145–1147, (2003).

[81] J. M. Martel and M. Toner, "Inertial focusing dynamics in spiral microchannels," *Physics of Fluids*, vol. 24, no. 3, p. 032001, (2012).

[82] D. R. Gossett, H. T. K. Tse, S. A. Lee, Y. Ying, A. G. Lindgren, O. O. Yang, J. Rao, A. T. Clark, and D. Di Carlo, "Hydrodynamic stretching of single cells for large population mechanical phenotyping," *Proceedings of the National Academy of Sciences*, vol. 109, pp. 7630–7635, May 2012.

[83] K. S. Paulsen, D. Di Carlo, and A. J. Chung, "Optofluidic fabrication for 3D-shaped particles," *Nature Communications*, vol. 6, no. 1, p. 2066, (2015).